

Discovery in Drell-Yan Processes at the LHC

Cheng-Wei Chiang^{1,2,3,4}, Neil D. Christensen^{4,5}, Gui-Jun Ding⁶, and Tao Han^{4,5}

¹ *Department of Physics and Center for Mathematics and Theoretical Physics,
National Central University, Chungli, Taiwan 32001, ROC*

² *Institute of Physics, Academia Sinica, Taipei, Taiwan 11925, ROC*

³ *Physics Division, National Center for Theoretical Sciences, Hsinchu, Taiwan 30043, ROC*

⁴ *Department of Physics, University of Wisconsin-Madison, Madison, WI 53706, USA*

⁵ *Department of Physics & Astronomy, University of Pittsburgh, Pittsburgh, PA 15260, USA*

⁶ *Department of Modern Physics, University of Science and Technology of China, Hefei, Anhui 230026, PRC*

We study the Drell-Yan process mediated by a new bosonic resonance at the LHC. The bosons of spin-0, 1, and 2 with the most general leading-order couplings to Standard Model fermions and gluons are considered, which provide a model-independent formulation for future exploration of the resonance properties, such as its spin, mass and couplings. In the case of neutral resonances, we demonstrate how the shapes of the kinematical distributions change as one varies the chiral couplings of the quarks and leptons, and show how to analyze the couplings by making use of the forward-backward asymmetry. In the case of charged resonances, we propose a novel technique to effectively reconstruct the angular distribution in the center-of-mass frame, to a large extent avoiding the two-fold ambiguity due to the missing neutrino. Similar to the case of a neutral resonance, the spin information of the resonance can be extracted unambiguously, and chiral couplings and the asymmetries can be explored in a statistical manner. With the current LHC data, we present bounds on the mass and cross section times branching fraction of the new resonance and estimate the future reach.

I. INTRODUCTION

With the start of the LHC experiments, we have entered a new era of high-energy physics that directly probes Nature at the TeV scale. Depending on the underlying theory, new particles of different kinds may lead to novel and distinctive signatures at the collider. In addition to the highly anticipated discovery of the origin of electroweak symmetry breaking, we will likely also discover other new resonances associated with this scale, presumably through the classic Drell-Yan (DY) process with a striking signal at around the TeV scale. If such a new resonance is indeed observed, it is important to determine many of its properties, such as the spin J , fermionic chiral couplings, and so on, in addition to its mass, width and electric charge. In this work, we consider new spin-0, 1, and 2 resonances that can contribute to the s -channel Drell-Yan processes¹. In view of many possible models predicting such resonances, we keep the couplings between the standard model (SM) fermions and the resonances as general as allowed by symmetries.

For a new neutral resonance, the final state involves two charged leptons whose momentum information can be fully registered by the detector. Therefore, with a sufficient rate, the particle mass can be readily deter-

mined from the invariant mass distribution. By boosting to the center-of-mass (CM) frame of the two leptons and noting that the boost direction preferably coincides with the momentum of the colliding quark, one can study the angular distribution of the leptons to extract the spin information of the resonance.

The case of a charged resonance is more complicated. This is because the final state contains a charged lepton and the associated neutrino, thus missing energy is involved in such events. The resonance mass can be best determined from the Jacobian peak in the transverse mass distribution. However, there is a difficulty in finding the correct CM frame of the charged lepton and the neutrino. Even if one assumes that the resonance mass has been measured, there are generally two possible solutions for the longitudinal momentum of the neutrino. We develop a novel technique to effectively construct the angular distribution for the charged lepton in the CM frame in a statistical manner, and show how the spin and chiral couplings of the resonance can be extracted in a similar fashion as in the case of neutral resonances.

This paper is organized as follows. In Section II, we classify types of new resonances that can mediate s -channel Drell-Yan processes at the LHC, and discuss some of the general features of these processes. In addition, we discuss the most general interactions between SM fermions and the new resonances allowed by the Lorentz and gauge invariances, with the corresponding Feynman rules given in Appendix A. Section III is devoted to the discussions of the Drell-Yan process mediated by a neutral resonance. The Drell-Yan process associated with a charged resonance is analyzed in Sec-

¹ There have been many studies of resonances that can contribute to the Drell-Yan process. See, for example, [1–56], where [2–35] deal with a neutral boson, [36–45] deal with a charged boson and [46–56] deal with both.

tion IV. The current results of the LHC are used to place a bound on the masses and couplings of these new resonances in Section V. The findings of this work are summarized in Section VI. Appendix B contains details of the FeynRules implementation of these new interactions. Appendix C gives a short review of the Wigner $d_{m,m'}^j$ functions that are useful for the helicity amplitudes of our calculations.

II. GENERAL INTERACTIONS OF NEW DRELL-YAN RESONANCES

We will concentrate exclusively on color-singlet neutral-current and charged-current s -channel resonances contributing to the Drell-Yan processes at the LHC

$$pp \rightarrow \ell^+ \ell^- X \quad \text{and} \quad \ell^\pm \nu X, \quad (1)$$

where ℓ generically denotes either an electron or a muon, ν denotes a neutrino or an antineutrino and X the inclusive hadronic remnants. We consider the most general couplings for leading-order operators allowed by certain symmetries for such a new particle. This particle must be a color singlet and have integer spin. We concentrate on the possibilities of a scalar (S), vector (V) and traceless symmetric second-rank tensor (T), although other spins are possible in principle. There are two cases for the electrical charge of the boson. In the case of neutral-current processes, this boson (generically denoted by R_0) must be neutral whereas for the charged-current processes, this boson (generically denoted by R_c) must have charge ± 1 . In Table I, we summarize the properties of these new bosons along with the processes to which they contribute.

Notation	$ Q_e $	J	Partonic processes
R_0	0	0, 1, 2	$u\bar{u}, d\bar{d}, gg \rightarrow \ell^+ \ell^-$
R_c	1	0, 1, 2	$u\bar{d} \rightarrow \ell^+ \nu, d\bar{u} \rightarrow \ell^- \bar{\nu}$

TABLE I: Resonance particles, their quantum numbers, and s -channel Drell-Yan processes. Q_e and J represent their electric charge and spin respectively.

We now write down the most general Lagrangian between these new bosons and the SM fermions and gluons allowed by Lorentz, quantum chromodynamic and electromagnetic gauge invariance. In each case, we only include the leading effective terms which are either dimension-4 or dimension-5 operators. Furthermore, we drop all terms which vanish when the masses of the initial-state and final-state particles are taken to zero.

A. Spin-0 states

We begin with the neutral scalar boson S which can have the following Lagrangian

$$\mathcal{L}_S = \bar{f}_i \left(g_{Sij}^f + i g_{Pij}^f \gamma_5 \right) f_j S - \frac{1}{4} \frac{g_S^a}{\Lambda} F_{\mu\nu}^a F^{\mu\nu} S, \quad (2)$$

where f can be either a quark or a lepton. The indices i and j run over generations, and the generation matrices $g_{Sij}^f = (g_S^f)_{ij}$ and $g_{Pij}^f = (g_P^f)_{ij}$ are required to be Hermitian by the Hermiticity of the Lagrangian. $F_{\mu\nu}^a$ denotes the gluonic field strength tensor. Here and henceforth, Λ denotes the cutoff scale of the effective interactions, which should be at least at the order of the resonance mass or higher. For the charged scalar boson S^\pm , we have

$$\begin{aligned} \mathcal{L}_{S^\pm} = & \bar{u}_i \left(h_{Sij}^q + i h_{Pij}^q \gamma_5 \right) d_j S^+ + \text{h.c.} \\ & + \bar{\nu}_i \left(h_{Sij}^\ell + i h_{Pij}^\ell \gamma_5 \right) \ell_j S^+ + \text{h.c.}, \end{aligned} \quad (3)$$

where $h_{Sij}^f = (h_S^f)_{ij}$ and $h_{Pij}^f = (h_P^f)_{ij}$ are allowed to be general complex matrices.

B. Spin-1 states

Using the same notation, the most general Lagrangian for the neutral vector boson V_μ is

$$\mathcal{L}_V = \bar{f}_i \gamma^\mu \left(g_{Vij}^f + g_{Aij}^f \gamma_5 \right) f_j V_\mu, \quad (4)$$

where $g_{Vij}^f = (g_V^f)_{ij}$ and $g_{Aij}^f = (g_A^f)_{ij}$ are required to be Hermitian matrices.² We have dropped interactions of the neutral vector boson V with gluons since they do not contribute to this Drell-Yan process. The charged vector boson has the Lagrangian

$$\begin{aligned} \mathcal{L}_{V^\pm} = & \bar{u}_i \gamma^\mu \left(h_{Vij}^q + h_{Aij}^q \gamma_5 \right) d_j V_\mu^+ + \text{h.c.} \\ & + \bar{\nu}_i \gamma^\mu \left(h_{Vij}^\ell + h_{Aij}^\ell \gamma_5 \right) \ell_j V_\mu^+ + \text{h.c.}, \end{aligned} \quad (5)$$

where $h_{Vij}^f = (h_V^f)_{ij}$ and $h_{Aij}^f = (h_A^f)_{ij}$ are allowed to be general complex matrices.

C. Spin-2 states

The neutral tensor Lagrangian is given by

$$\mathcal{L}_T = \frac{i}{\Lambda} \left[\bar{f}_i \left(g_{Tij}^f - g_{ATij}^f \gamma_5 \right) (\gamma^\mu \partial^\nu f_j + \gamma^\nu \partial^\mu f_j) \right]$$

² Our convention is fixed with respect to the SM couplings as $g_{ZV}^f = g_Z (\frac{1}{2} T_3^f - Q^f s_w^2)$, $g_{ZA}^f = -\frac{1}{2} T_3^f g_Z$, where $g_Z = g/c_w$, g is the weak coupling and s_w and c_w are the sine and cosine of the Weinberg angle. The left- and right-chiral couplings are related to the vector and axial-vector couplings as $g_{RXL} = g_{RXV} - g_{RXA}$, $g_{RXR} = g_{RXV} + g_{RXA}$.

$$\begin{aligned}
& -(\partial^\mu \bar{f}_i \gamma^\nu + \partial^\nu \bar{f}_i \gamma^\mu) \left(g_{Tij}^{f\dagger} + g_{ATij}^{f\dagger} \gamma_5 \right) f_j \Big] T_{\mu\nu} \\
& - \frac{1}{4} \frac{g_T^g}{\Lambda} F_{\mu\alpha}^a F_\beta^{a\mu} T^{\alpha\beta}, \tag{6}
\end{aligned}$$

where the couplings $g_{Tij}^f = (g_T^f)_{ij}$ and $g_{ATij}^f = (g_{AT}^f)_{ij}$ are general 3×3 complex matrices. Note that a dimension-4 operator between SM fermions and neutral tensor particle is not allowed since it would be proportional to the trace of the tensor which we have assumed to be traceless. Finally, the charged tensor has the interaction Lagrangian as follows

$$\begin{aligned}
\mathcal{L}_{T^\pm} = & \frac{i}{\Lambda} \left[\bar{u}_i \left(h_{Tij}^q - h_{ATij}^q \gamma_5 \right) (\gamma^\mu \partial^\nu d_j + \gamma^\nu \partial^\mu d_j) \right. \\
& \left. - (\partial^\mu \bar{u}_i \gamma^\nu + \partial^\nu \bar{u}_i \gamma^\mu) \left(\tilde{h}_{Tij}^q + \tilde{h}_{ATij}^q \gamma_5 \right) d_j \right] T_{\mu\nu}^+ \\
& + \frac{i}{\Lambda} \left[\bar{\nu}_i \left(h_{Tij}^\ell - h_{ATij}^\ell \gamma_5 \right) (\gamma^\mu \partial^\nu \ell_j + \gamma^\nu \partial^\mu \ell_j) \right. \\
& \left. - (\partial^\mu \bar{\nu}_i \gamma^\nu + \partial^\nu \bar{\nu}_i \gamma^\mu) \left(\tilde{h}_{Tij}^\ell + \tilde{h}_{ATij}^\ell \gamma_5 \right) \ell_j \right] T_{\mu\nu}^+ \\
& + \text{h.c.}, \tag{7}
\end{aligned}$$

where $h_{Tij}^f = (h_T^f)_{ij}$, $h_{ATij}^f = (h_{AT}^f)_{ij}$, $\tilde{h}_{Tij}^f = (\tilde{h}_T^f)_{ij}$ and $\tilde{h}_{ATij}^f = (\tilde{h}_{AT}^f)_{ij}$ are general complex matrices. The corresponding Feynman rules have been worked out and can be found in Appendix A.

III. NEUTRAL BOSON RESONANCES

Diagrams for the Drell-Yan process $pp \rightarrow \ell^+ \ell^- X$ mediated by a neutral boson at tree level are shown in Fig. 1, including the SM diagrams with γ/Z exchanges. The corresponding helicity amplitudes are listed in Table II where

$$D_X = s - M_X^2 + iM_X \Gamma_X. \tag{8}$$

We have expressed the scattering amplitudes in terms of the Wigner $d_{m,m'}^j$ functions, where j is the total angular momentum and m and m' are the difference of the helicities of the initial-state and final-state particles, respectively [57]. A short review of the $d_{m,m'}^j$ functions can be found in Appendix C. For s -channel scalar resonances, the initial state particles must have the same helicities to conserve angular momentum. The same is true for the final state particles. For this reason, we find that only the helicity combinations $(\lambda, \lambda) \rightarrow (\lambda', \lambda')$ are nonzero. On the other hand, for s -channel vector and tensor interactions, angular momentum is not sufficient to determine the helicity combinations of the external particles. However, the combined effect of the masslessness of the external fields and the properties of the interaction vertices only allows opposite helicities for the incoming particles and also for the outgoing particles $(\lambda, -\lambda) \rightarrow (\lambda', -\lambda')$.

A. Invariant mass spectrum

The best observable to discover a new neutral boson coupling to quarks and charged leptons is in the spectrum of the invariant mass

$$M_{\ell\ell}^2 = (p_{\ell^+} + p_{\ell^-})^2, \tag{9}$$

If there is no interference, the shape of the invariant mass distribution is of a Breit-Wigner form and peaked at the mass of the new boson. However, if there is significant interference between the new resonance and the SM diagrams, there can be appreciable changes in the shape. In particular, the peak may even be shifted. We show the di-lepton invariant mass distribution in Fig. 2 for the process $pp \rightarrow \ell^+ \ell^- X$, only including the subprocess $u\bar{u} \rightarrow \ell^+ \ell^-$, mediated by a scalar (green dot-dashed), vector (red dotted) and tensor (blue dashed) boson, along with the SM (black solid) contributions including the full spin correlations. To see the interference effects clearly, we have adjusted the resonance rate to be the same value as the SM background rate near the peak. The row and column headers specify the nature of the chiral couplings. (The scalar fields have a factor of i accompanying the γ_5 .) Here and henceforth, for illustration, the mass of the new particle is taken to be 1 TeV while the width is taken to be 20 GeV. We adopt the parton distribution functions (PDF's) CTEQ6L [58]. The LHC energy is set at 7 TeV unless stated otherwise.

For massless fermions, the scalar particle amplitude (\mathcal{M}_S) is nonzero only for initial and final states of the same helicity while the SM contribution is nonzero only for initial and final states of opposite helicities. For this reason, there is never any interference between the two, and a scalar field always renders a Breit-Wigner shape peaked at the mass of the scalar particle. This can be seen analytically in Table II, and also numerically in the dot-dashed (green) curves of Fig. 2.

The new vector boson does interfere with the SM. The amount of interference depends on the parity properties of the couplings. The interference always flips sign at the mass of the new boson due to the phase change in the propagator $s - M_V^2$. In addition, there is an overall sign coming from the couplings. After summing over helicities and integrating over the scattering angle θ , we find that the interference with the SM photon diagram is given by

$$\sum_{hel} \int_{-1}^1 d\cos\theta (\mathcal{M}_\gamma \mathcal{M}_V^* + \mathcal{M}_\gamma^* \mathcal{M}_V) \propto \mathcal{R}(g_{Vmi}^q g_{Vjn}^\ell), \tag{10}$$

where $\mathcal{R}(x)$ means the real part of x . The interference with the photon is independent of parity violation and only depends on the sign of the vectorial coupling. The interference with the Z boson diagram, on the other hand, is given by

$$\begin{aligned}
& \sum_{hel} \int_{-1}^1 d\cos\theta (\mathcal{M}_Z \mathcal{M}_V^* + \mathcal{M}_Z^* \mathcal{M}_V) \propto \\
& \mathcal{R}[(g_{ZV}^q g_{Vmi}^q + g_{ZA}^q g_{Ami}^q)(g_{ZV}^\ell g_{Vjn}^\ell + g_{ZA}^\ell g_{Ajn}^\ell)], \tag{11}
\end{aligned}$$

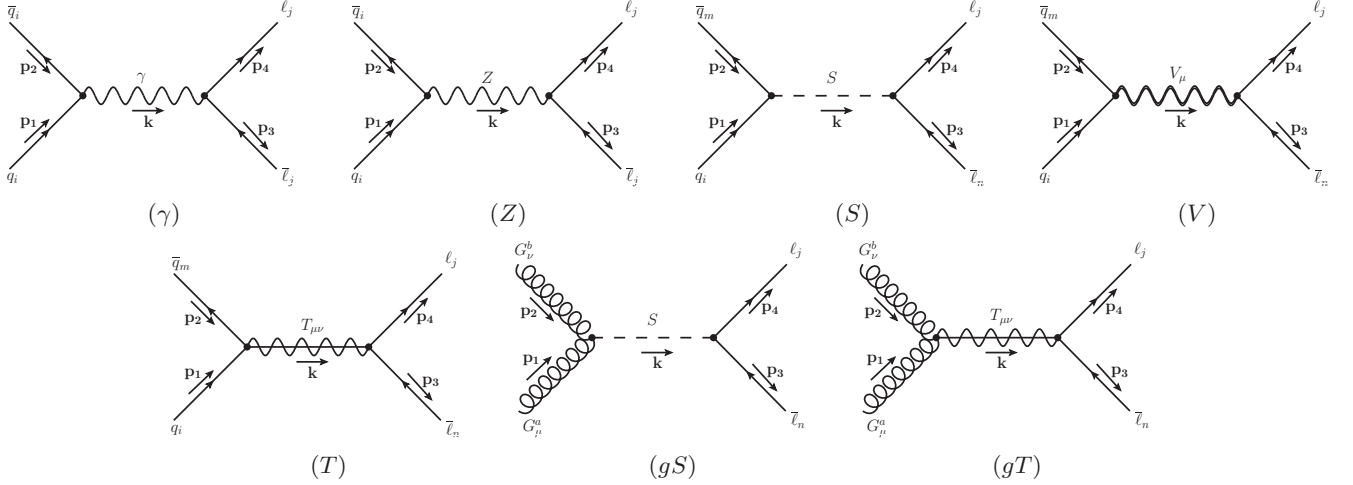


FIG. 1: The s -channel Feynman diagrams responsible for $pp \rightarrow \ell^+ \ell^- X$. Contributions to $\bar{q}q \rightarrow \ell^+ \ell^-$ are from a photon (γ), a Z boson (Z), a new scalar particle (S), a new vector particle (V) and a new tensor particle (T). Contributions to $gg \rightarrow \ell^+ \ell^-$ are from a new scalar field (gS) and a new tensor field (gT).

which has more complicated dependence on the vector and axial vector couplings. Since g_{ZV}^ℓ is very small, the sign of the interference is more strongly dependent on the axial coupling to leptons. Again, the interference can be seen analytically in Table II and numerically in the dotted (red) curves of Fig. 2.

In the case of the tensor field, the term proportional to $d_{m,m'}^2$ does not contribute to interference in the invariant mass distribution since $d_{m,m'}^2$ is orthogonal to $d_{m,m'}^1$, and this interference vanishes after integration over θ . The $d_{m,m'}^1$ term of the tensor amplitude is due to the off-shell effects and does not contribute to the peak at $M_{\ell\ell} = M_V$. Consequently, the interference is very weak and not readily observable in the continuum invariant mass distribution. The final result is that the tensor boson has a Breit-Wigner shape peaked at its mass as can be seen in the dashed (blue) curves of Fig. 2, which is hardly distinguishable from the case of a scalar.

B. Transverse momentum distribution

Once a new boson resonance is established in the invariant mass spectrum, it will be of ultimate importance to study its other quantum numbers, such as its spin, chiral couplings, etc. For a massless particle, the transverse momentum is related to the scattering angle

$$p_T = E \sin \theta. \quad (12)$$

Thus, the differential distribution of p_T may contain additional information of chiral interactions of the resonance via the interference with the SM diagrams. We present the transverse momentum distribution of the negatively charged lepton for a variety of parity violation cases in Fig. 3. As expected, there is no interference between a spin-0 state and the SM diagrams. The fact

that a spin-2 resonance interferes with the SM in the transverse momentum distribution gives us a potential new way of determining the spin of the resonance, unlike the invariant mass distribution. If we find interference present in both the invariant mass distribution and the transverse momentum distribution, we can conclude that the new resonance is a spin-1 particle. Furthermore, the amount of interference and the sign of the interference can give information about the size and sign of the parity violation in the couplings. We emphasize that the analysis of the p_T distribution does not require a knowledge of the quark moving direction, nor the reconstruction of the CM frame.

C. Angular distribution

One of the main advantages of the present process is the feasibility to fully reconstruct the CM system of the two charged leptons that is the rest frame of the new boson. Although we do not know the direction of the quark on an event-by-event basis, it is strongly correlated with the direction of the CM frame of the charged lepton pair due to the parton distribution functions of the quark versus the anti-quark in a proton [46]. We calculate this angle by first boosting into the CM frame of the charged leptons, and then taking the angle between the moving direction of the negatively charged lepton and the direction of the boost. In the case of the gluon initial state, both directions are equally valid and we simply use the direction of the boost to measure the negatively charged lepton as in the quark case.

The angular dependence comes from the Wigner $d_{m,m'}^j$ functions. For each helicity combination and each spin for the new boson, these are determined by the kinematics (see Appendix C). The mixture of the $d_{m,m'}^j$ functions

$q_i(\lambda)\bar{q}_m(-\lambda) \rightarrow \ell_j(\lambda')\bar{\ell}_n(-\lambda')$	
$\mathcal{M}_\gamma^{\lambda\lambda'} = \mathcal{N}_\gamma^{\lambda\lambda'} d_{1,\lambda\lambda'}^1$	$\mathcal{N}_\gamma^{\lambda\lambda'} = 8\pi\alpha\lambda\lambda'Q_q$
$\mathcal{M}_Z^{\lambda\lambda'} = \mathcal{N}_Z^{\lambda\lambda'} d_{1,\lambda\lambda'}^1$	$\mathcal{N}_Z^{\lambda\lambda'} = -\frac{2s}{D_Z}(\lambda g_{ZV}^q + g_{ZA}^q)(\lambda' g_{ZV}^\ell + g_{ZA}^\ell)$
$\mathcal{M}_V^{\lambda\lambda'} = \mathcal{N}_V^{\lambda\lambda'} d_{1,\lambda\lambda'}^1$	$\mathcal{N}_V^{\lambda\lambda'} = -\frac{2s}{D_V}(\lambda g_V^q + g_A^q)_{mi}(\lambda' g_V^\ell + g_A^\ell)_{jn}$
$\mathcal{M}_T^{\lambda\lambda'} = \mathcal{N}_{T2}^{\lambda\lambda'} d_{1,\lambda\lambda'}^2 + \mathcal{N}_{T1}^{\lambda\lambda'} d_{1,\lambda\lambda'}^1$	$\mathcal{N}_{T2}^{\lambda\lambda'} = -\frac{2\lambda\lambda's^2}{\Lambda^2 D_T} \mathcal{H}_+(g_T^q + \lambda g_{AT}^q)_{mi} \mathcal{H}_+(g_T^\ell + \lambda' g_{AT}^\ell)_{jn}$
	$\mathcal{N}_{T1}^{\lambda\lambda'} = \frac{2\lambda\lambda's^2(s-M_T^2)}{\Lambda^2 M_T^2 D_T} \mathcal{H}_-(g_T^q + \lambda g_{AT}^q)_{mi} \mathcal{H}_-(g_T^\ell + \lambda' g_{AT}^\ell)_{jn}$
$g^a(\lambda)g^b(-\lambda) \rightarrow \ell_j(\lambda')\bar{\ell}_n(-\lambda')$	
$\mathcal{M}_{gT}^{\lambda\lambda'} = \mathcal{N}_{gT}^{\lambda\lambda'} d_{1,\lambda\lambda'}^2$	$\mathcal{N}_{gT}^{\lambda\lambda'} = -\frac{\lambda\lambda'g_T^q s^2}{2\Lambda^2 D_T} \mathcal{H}_+(g_{Tjn}^\ell + \lambda' g_{ATjn}^\ell) \delta^{ab}$
$q_i(\lambda)\bar{q}_m(\lambda) \rightarrow \ell_j(\lambda')\bar{\ell}_n(\lambda')$	
$\mathcal{M}_S^{\lambda\lambda'} = \mathcal{N}_S^{\lambda\lambda'} d_{0,0}^0$	$\mathcal{N}_S^{\lambda\lambda'} = \frac{s}{D_S}(i\lambda g_{Smi}^q - g_{Pmi}^q)(i\lambda' g_S^\ell + g_P^\ell)_{jn}$
$g^a(\lambda)g^b(\lambda) \rightarrow \ell_j(\lambda')\bar{\ell}_n(\lambda')$	
$\mathcal{M}_{gS}^{\lambda\lambda'} = \mathcal{N}_{gS}^{\lambda\lambda'} d_{0,0}^0$	$\mathcal{N}_{gS}^{\lambda\lambda'} = \frac{g_S^q s^{3/2}}{2\Lambda D_S}(\lambda' g_S^\ell - i g_P^\ell)_{jn} \delta^{ab}$

TABLE II: Helicity scattering amplitudes for the parton-level processes. The amplitudes correspond to the diagrams in Fig. 1. The particles in the s -channel exchange are labelled by subscripts (γ , Z , S , V and T) while gS and gT indicate that the initial states are gluons with scalar and tensor exchange, respectively. λ and λ' are the helicities and we define $\mathcal{H}_\pm(M) = M \pm M^\dagger$.

encodes the information of its spin and chiral interactions. For the scalar field, only $d_{0,0}^0$ contributes and so the angular distribution is flat. This can be seen in the dot-dashed (green) curves of Fig. 4. For a vector field, the $d_{\pm 1, \pm 1}^1$ functions contribute. Each one is squared and summed with the appropriate factors (see Table II). This gives the angular distribution

$$\begin{aligned} \overline{\sum} |\mathcal{M}_V|^2 &= \frac{4s^2}{|D_V|^2} \left[A_V (1 + \cos \theta)^2 + B_V (1 - \cos \theta)^2 \right], \\ A_V &= (g_{VR}^q g_{VR}^\ell)^2 + (g_{VL}^q g_{VL}^\ell)^2, \\ B_V &= (g_{VR}^q g_{VL}^\ell)^2 + (g_{VL}^q g_{VR}^\ell)^2. \end{aligned} \quad (13)$$

This is the formula of a parabola versus $\cos \theta$ where the amount of parity violation determines where the minimum lies. This parabolic shape can be seen in the dotted (red) curves of Fig. 4. We find that the angular distribution is symmetric whenever either coupling is pure vector or axial vector. If both the quark and the lepton couplings are parity-violating (mixtures of 1 and γ_5 terms), then the angular distribution is shifted to one side or the other. The shift is maximal when both couplings are purely chiral (the magnitude of the vector coupling equals

that of the axial coupling, as in $1 \pm \gamma_5$). However, it is interesting to note that the distributions are identical for either purely right-handed or purely left-handed, and are parity-transformed for right- and left-mixed couplings.

For the tensor field, the angular dependence is mainly a mixture of the $d_{\pm 1, \pm 1}^2$ functions (the $d_{\pm 1, \pm 1}^1$ functions give a small perturbation)

$$\begin{aligned} \overline{\sum} |\mathcal{M}_T|^2 &= \frac{16s^4}{\Lambda^4 |D_T|^2} \left[A_T (1 + \cos \theta)^2 (2 \cos \theta - 1)^2 \right. \\ &\quad \left. + B_T (1 - \cos \theta)^2 (2 \cos \theta + 1)^2 \right], \end{aligned}$$

where A_T and B_T are of the same form as in Eq. (13), but with the tensor couplings. This is a quartic function with one local maximum and two local minima, a “W” shape. It can be seen in the dashed (blue) curves of Fig. 4. In particular, we find that if either of the couplings are purely tensor ($g \propto 1$) or purely axial tensor ($g \propto \gamma_5$) the distribution is symmetric, with the local maximum occurring at $\cos \theta = 0$. However, if both quark and lepton couplings are mixtures of 1 and γ_5 , then the curves shift toward one side or the other, leading to parity violation. As in the vector case, the shift is maximal when

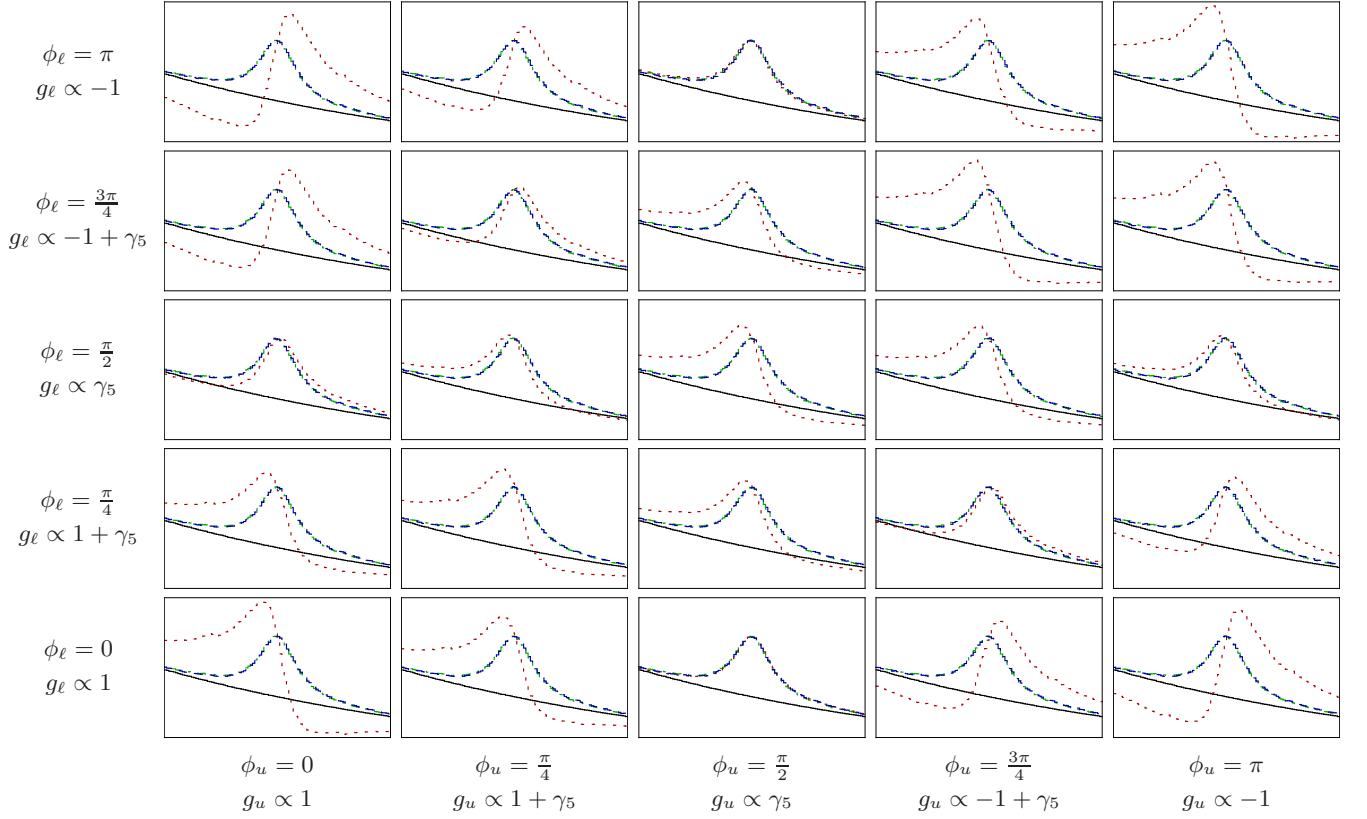


FIG. 2: (Color online) Invariant mass distribution for the process $pp \rightarrow \ell^+ \ell^- X$. The vertical axis is the differential cross section in arbitrary units and the horizontal axis is the dilepton invariant mass running from 950 GeV to 1050 GeV. The row and column headers specify the nature of the chiral couplings. The solid (black) curve is for the SM, the dot-dashed (green) curve includes the scalar field, the dotted (red) curve includes the vector field, and the dashed (blue) curve includes the tensor field. The scalar and tensor curves are indistinguishable and right on top of each other. The mass of the new particle is taken to be 1 TeV while the width is taken to be 20 GeV. The LHC energy is set at 7 TeV, and the CTEQ6L PDF sets are used.

the coefficient of 1 has the same magnitude as that of γ_5 .

To be more realistic, we fold in the CTEQ6L parton distribution functions and adopt some basic acceptance cuts on the transverse momentum and its pseudo-rapidity for the charged leptons

$$p_{T\ell} > 20 \text{ GeV}, \quad |\eta_\ell| < 2.5. \quad (14)$$

We see the effects in the three panels on the right-hand side in Fig. 4. Due to the misidentification of the correct quark momentum direction, the far forward/backward regions are diluted. The rapidity cut limits the angle reach in the same region as seen at the drop near 0.8.

D. Forward-backward asymmetry

It is customary to construct the forward-backward asymmetry, based on the partially integrated rates in the opposite angular regions, which can be defined as

$$A_{FB}(c_0) = \frac{N(\cos\theta > c_0) - N(\cos\theta < -c_0)}{N(\cos\theta > c_0) + N(\cos\theta < -c_0)}. \quad (15)$$

$c_0 = 0$ will lead to the largest event rate, while a particular choice of c_0 may optimize the size of the asymmetry³.

It is clear that a scalar field will give $A_{FB} = 0$ for any value of c_0 since it has a flat angular distribution.

For a vector field, it is natural to use $c_0 = 0$. It can be shown that the forward-backward asymmetry at the peak of a vector resonance is given by

$$\begin{aligned} A_{FB}^V &= A_{FB}(0) = \frac{3}{4} \frac{A_V - B_V}{A_V + B_V} \\ &= \frac{3g_V^q g_V^\ell g_A^q g_A^\ell}{[(g_V^q)^2 + (g_A^q)^2][(g_V^\ell)^2 + (g_A^\ell)^2]} = \frac{3}{4} \sin 2\phi_q \sin 2\phi_\ell, \end{aligned} \quad (16)$$

where ϕ_f defines the ratio of vector and axial couplings

³ The asymmetry can be defined with any differential form with respect to the angular range. Other Lorentz invariant asymmetries have also been proposed, for example [59, 60]. Others have noted that the asymmetry can be used to discriminate between different Z' models [3, 6, 27, 31, 61–66].

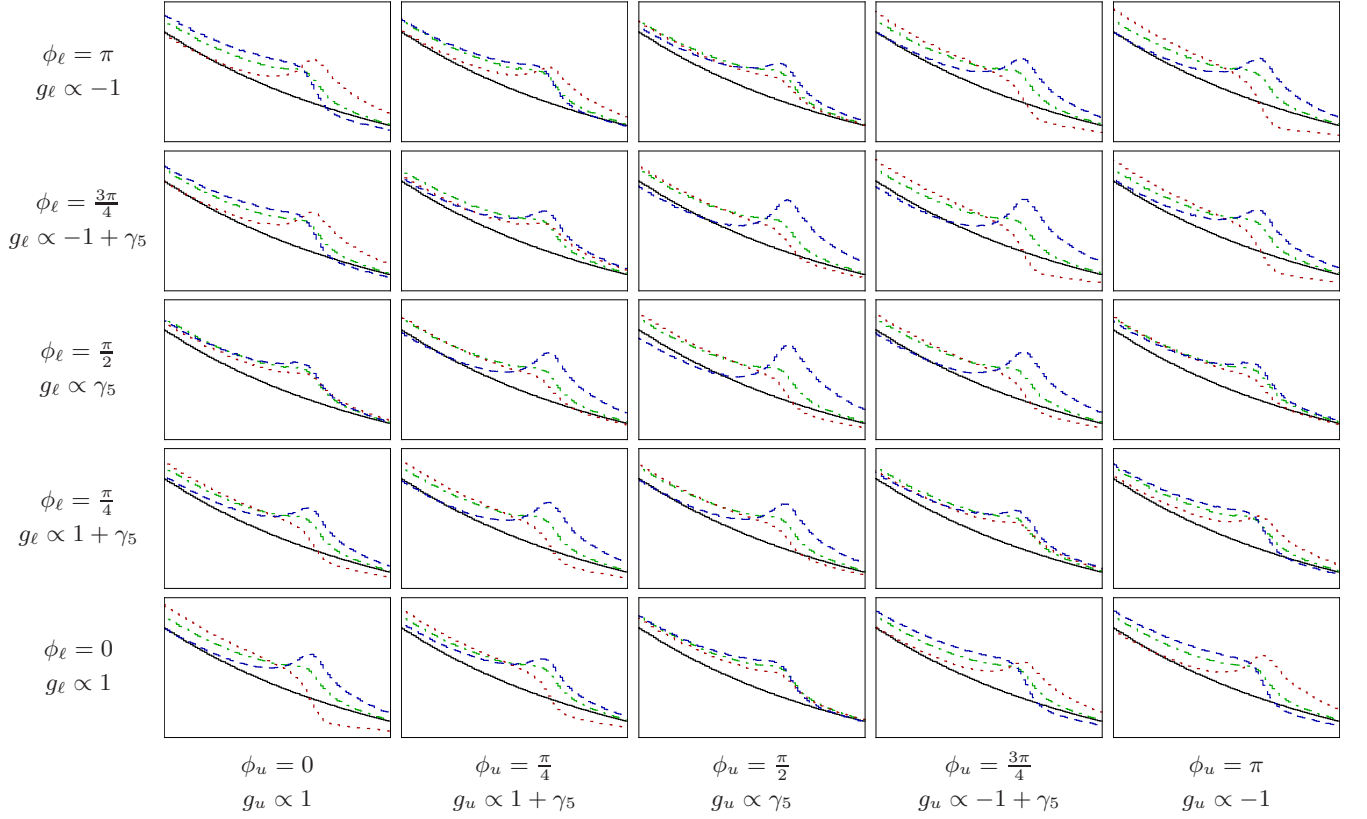


FIG. 3: (Color online) Transverse momentum distribution of ℓ^- for the process $pp \rightarrow \ell^+ \ell^- X$. The vertical axis is the differential cross section in arbitrary units and the horizontal axis is the transverse momentum running from 450 GeV to 525 GeV. The row and column headers specify the nature of the chiral couplings. The curve legends are the same as in Fig. 2.

and is given by

$$\cos \phi_f = \frac{g_V^f}{\sqrt{(g_V^f)^2 + (g_A^f)^2}}, \quad \sin \phi_f = \frac{g_A^f}{\sqrt{(g_V^f)^2 + (g_A^f)^2}}.$$

For example, $\phi_f = 0$ corresponds to a pure vector coupling with $g^f \propto 1$, $\phi_f = \pi/4$ corresponds to a pure chiral coupling with $g^f \propto 1 + \gamma_5$, and so on. Eq. (16) shows that the absolute value of the asymmetry is bounded to be less than or equal to $3/4$. Also, if any of the couplings g_V^q, g_A^q, g_V^ℓ and g_A^ℓ is identically zero, there is no forward-backward asymmetry, resulting in parity conservation. The SM asymmetry for the $u\bar{u} \rightarrow \ell^+ \ell^-$ process at $\sqrt{s} \gg M_Z$ is approximately 0.6. As mentioned before, the quark momentum direction is ambiguous in pp collisions. We thus take the angle in the CM frame with respect to the boost direction, which is more likely to be the direction of the quark.

Again, to be more realistic, we convolute with the parton distribution functions, and take the acceptance cuts as in Eq. (14). In Fig. 5(a) and 5(b), we present the equal-valued contours of forward-backward asymmetry for a vector resonance in the $\phi_u^V - \phi_\ell^V$ plane. Fig. 5(a) shows contours for $u\bar{u} \rightarrow \ell^+ \ell^-$ via the resonance only, and Fig. 5(b) includes the PDF convolution at the hadronic level.

We see that the asymmetry is reduced when the parton distribution functions are turned on and acceptance cuts imposed. The SM value becomes ~ 0.37 . As for the signal, the maximum is reduced from $3/4$ to ~ 0.41 . The reason for this is that the boost direction corresponds with the quark direction much of the time but is sometimes in the opposite direction. The asymmetry breaks up into quadrants separated by the angles $\phi^V = n\pi/2$ for some integer n where the asymmetry is 0. This is where the sign of the vectorial or axial coupling changes sign, thus changing the sign of the asymmetry.

For a tensor particle, we find that $c_0 \neq 0$ is required to obtain a non-zero asymmetry. This can be seen by noting that for $c_0 = 0$,

$$\begin{aligned} & \int_{-1}^0 d\cos\theta \left[A_T (1 + \cos\theta)^2 (2\cos\theta - 1)^2 \right. \\ & \quad \left. + B_T (1 - \cos\theta)^2 (2\cos\theta + 1)^2 \right] \\ &= \int_0^1 d\cos\theta \left[A_T (1 + \cos\theta)^2 (2\cos\theta - 1)^2 \right. \\ & \quad \left. + B_T (1 - \cos\theta)^2 (2\cos\theta + 1)^2 \right] \end{aligned}$$

for all values of A_T and B_T . In other words, although the tensor distribution is asymmetric, it always shifts in

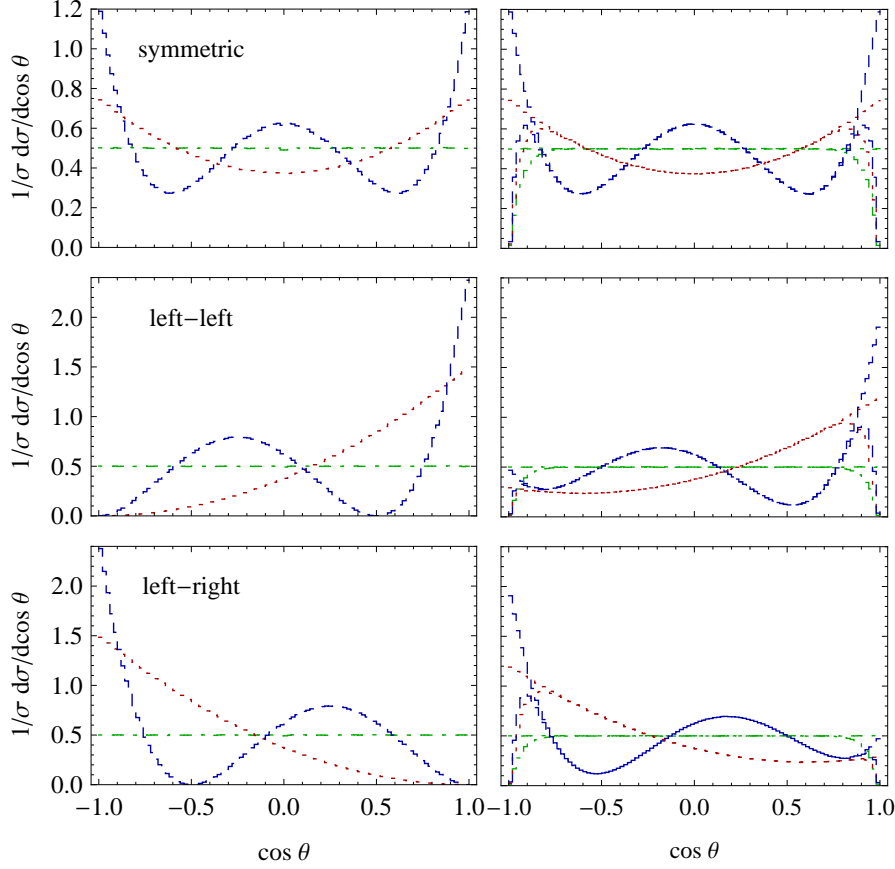


FIG. 4: (Color online) Angular distributions of ℓ^- in the CM frame for the process $pp \rightarrow \ell^+ \ell^- X$. The curve legends are the same as in Fig. 2. In the top row purely scalar, vectorial and tensorial couplings are used. In the second row left chiral couplings are used while in the third row left chiral couplings are used for the quark but right chiral couplings are used for the leptons. In the left column the PDF's are turned off and the lab frame is the same as the CM frame, while on the right, the PDF's are turned on and the boost direction is used. On the right panels, the visible bend-down feature in the forward-backward regions is due to the kinematical cuts as described in the text.

such a way as to have equal area under the angular distribution for positive and negative values of $\cos\theta$. For this reason, it is necessary to use $c_0 \neq 0$. We find that the difference is maximized when $c_0 = 1/\sqrt{2}$.

$$\begin{aligned}
 A_{FB}^T &= A_{FB} \left(\frac{1}{\sqrt{2}} \right) \\
 &= \frac{5}{16 - 7\sqrt{2}} \frac{A_T - B_T}{A_T + B_T} \\
 &= \frac{20}{16 - 7\sqrt{2}} \frac{g_T^q g_T^\ell g_{AT}^q g_{AT}^\ell}{[(g_T^q)^2 + (g_{AT}^q)^2] [(g_T^\ell)^2 + (g_{AT}^\ell)^2]} \\
 &= \frac{5}{16 - 7\sqrt{2}} \sin 2\phi_q^T \sin 2\phi_\ell^T, \quad (17)
 \end{aligned}$$

where ϕ_f^T defines the ratio of tensor and axial tensor couplings, similar to the vector case. Similar to Figs. 5(a) and 5(b), the equal-valued contours of forward-backward asymmetry for a tensor resonance are presented in Figs 5(c) and 5(d). We again see that the asymmetry is reduced when the parton distribution functions

are turned on. The maximum asymmetry is reduced to a little greater than ~ 0.37 . The sign is similar to the vector case.

If an experiment discovers a resonance in the invariant mass distribution of the neutral Drell-Yan process, measuring the forward-backward asymmetry could help distinguish the spins in the early days before enough events are accumulated for reconstructing the angular distribution. If a significant asymmetry is found in $A_{FB}(0)$, this would be evidence of a new vector resonance. If no asymmetry is found in $A_{FB}(0)$, then one should further determine $A_{FB}(1/\sqrt{2})$. If $A_{FB}(1/\sqrt{2})$ is significantly different from zero while $A_{FB}(0) = 0$, then this would be evidence of a new tensor particle. If both are zero, then this is evidence for a symmetric distribution, but could come from any of the spins we have discussed here.

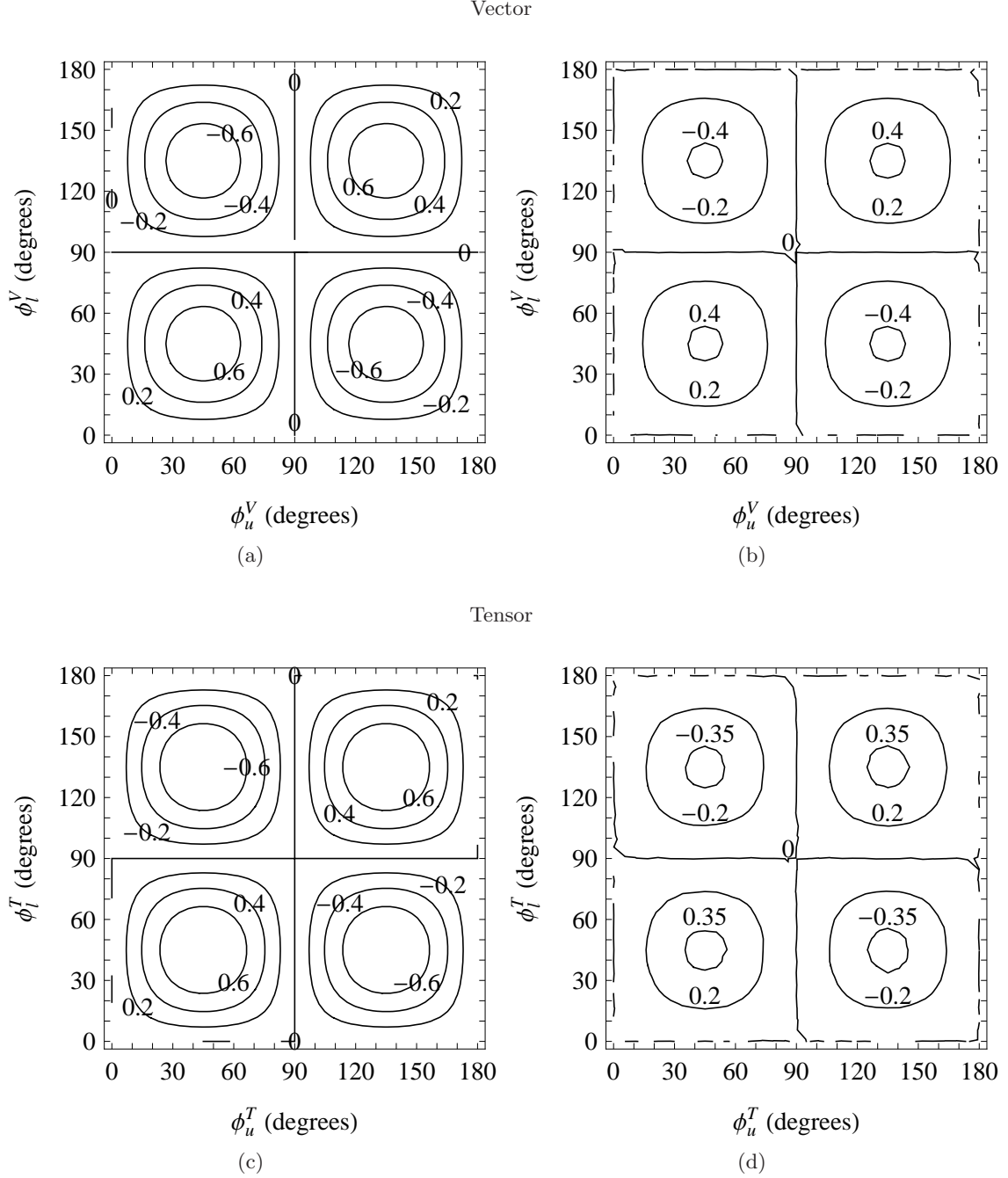


FIG. 5: Contours of forward-backward asymmetry labelled by the values of A_{FB} in the $u\bar{u} \rightarrow \ell^+\ell^-$ process. In the first row (a) and (b), a vector resonance is presented and in the second row (c) and (d), a tensor resonance is presented. Plots (a) and (c) show the result with the new physics amplitude alone in the lab frame while plots (b) and (d) include the PDF's and acceptance cuts.

IV. CHARGED BOSON RESONANCE

Charged bosons contribute to the Drell-Yan process $pp \rightarrow \ell^\pm \nu X$ through the diagrams in Fig. 6 at tree level. The resulting amplitudes are shown in Table III.

A. Transverse mass distribution

The first place we will look for a charged boson in Drell-Yan processes is in the transverse mass. Since we can not detect the neutrino, we can not fully reconstruct the invariant mass of the lepton system. The best one

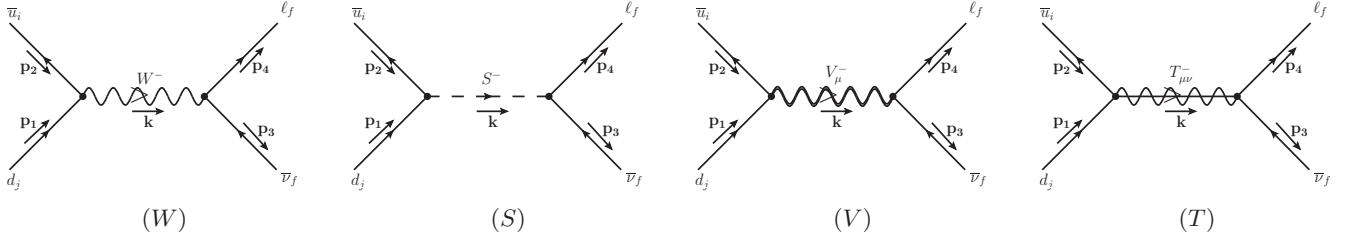


FIG. 6: The s -channel Feynman diagrams responsible for $pp \rightarrow \ell \bar{\nu} X$. Contributions to this process are from a W boson (W), a new scalar particle (S), a new vector particle (V) and a new tensor particle (T).

$d_i(\lambda)\bar{u}_m(-\lambda) \rightarrow \ell_j(\lambda')\bar{\nu}_n(-\lambda')$	
$\mathcal{M}_W^{\lambda\lambda'} = \mathcal{C}_W^{\lambda\lambda'} \delta_{\lambda',-1} d_{1,1}^1$	$\mathcal{C}_W^{\lambda\lambda'} = -\frac{g_W^2 V_{ij}^{KM} s}{D_W} \delta_{\lambda,-1}$
$\mathcal{M}_V^{\lambda\lambda'} = \mathcal{C}_V^{\lambda\lambda'} d_{1,\lambda\lambda'}^1$	$\mathcal{C}_V^{\lambda\lambda'} = -\frac{2s}{D_{V\pm}} (\lambda h_V^q + h_A^q)_{mi} (\lambda' h_V^{\ell\dagger} + h_A^{\ell\dagger})_{jn}$
$\mathcal{M}_T^{\lambda\lambda'} = \mathcal{C}_{T2}^{\lambda\lambda'} d_{1,\lambda\lambda'}^2 + \mathcal{C}_{T1}^{\lambda\lambda'} d_{1,\lambda\lambda'}^1$	$\mathcal{C}_{T2}^{\lambda\lambda'} = -\frac{2\lambda\lambda' s^2}{\Lambda^2 D_{T\pm}} \mathcal{T}_+(h_T^q + \lambda h_{AT}^q)_{mi} \mathcal{T}_+(h_T^{\ell\dagger} + \lambda' h_{AT}^{\ell\dagger})_{jn}$
	$\mathcal{C}_{T1}^{\lambda\lambda'} = -\frac{2\lambda\lambda' s^2 (s - M_{T\pm}^2)}{\Lambda^2 M_{T\pm}^2 D_{T\pm}} \mathcal{T}_-(h_T^q + \lambda h_{AT}^q)_{mi} \mathcal{T}_-(h_T^{\ell\dagger} + \lambda' h_{AT}^{\ell\dagger})_{jn}$
$d_i(\lambda)\bar{u}_m(\lambda) \rightarrow \ell_j(\lambda')\bar{\nu}_n(\lambda')$	
$\mathcal{M}_S^{\lambda\lambda'} = \mathcal{C}_S^{\lambda\lambda'} d_{0,0}^0$	$\mathcal{C}_S^{\lambda\lambda'} = \frac{s}{D_{S\pm}} (i\lambda h_S^q - h_P^q)_{mi} (i\lambda' h_S^{\ell\dagger} + h_P^{\ell\dagger})_{jn}$

TABLE III: Helicity scattering amplitudes for the parton-level processes. The amplitudes correspond with the diagrams in Fig. 6. The particles in the s -channel exchange are labeled by subscripts (W , V , T and S). λ and λ' are the helicities and we define $\mathcal{T}_{\pm}(M) = M \pm \tilde{M}$ where \tilde{M} means that we replace h by \tilde{h} in M .

can do is to construct the transverse mass which contains the charged lepton momentum and the missing transverse momentum:

$$M_T^2 = (E_{T\ell} + E_{Tmiss})^2 - (\mathbf{p}_{T\ell} + \mathbf{p}_{Tmiss})^2, \quad (18)$$

where the transverse energy is defined as $E_T = \sqrt{M^2 + p_T^2}$, and p_{Tmiss} is identified as $p_{T\nu}$. In practice, we assume that the SM leptons are massless. Furthermore, in a $2 \rightarrow 2$ process in the absence of transverse motion, the missing transverse momentum is equal and opposite to that of the charged lepton. This allows us to simplify the transverse mass to $M_T = 2p_{T\ell}$. This transverse mass distribution develops a Jacobian peak at the mass of the resonance particle. We plot examples of transverse mass distributions for a variety of parity violation cases in Fig. 7. Once again, we see that the shape of the transverse mass distribution depends on the parity properties of the fermionic couplings⁴. Both the

vector and the tensor shapes are modified, due to the interference effects near the resonance peak, while the scalar shape remains fixed. This could be important in determining the mass of a new charged resonance. Moreover, the discovery of interference in the transverse mass distribution implies that the spin of the new resonant particle is greater than 0 while the sign and size of the interference can give information about the sign and size of the parity violation in the couplings. We emphasize that the analysis of the transverse mass distribution does not require a knowledge of the quark moving direction, nor the reconstruction of the CM frame.

B. Angular distribution

Unlike the case mediated by a neutral boson, the angular analysis is known to be difficult for the charged boson mediation due to the missing neutrino in the final state,

⁴ The importance of the transverse mass in determining the properties of the couplings has also been discussed in [67].

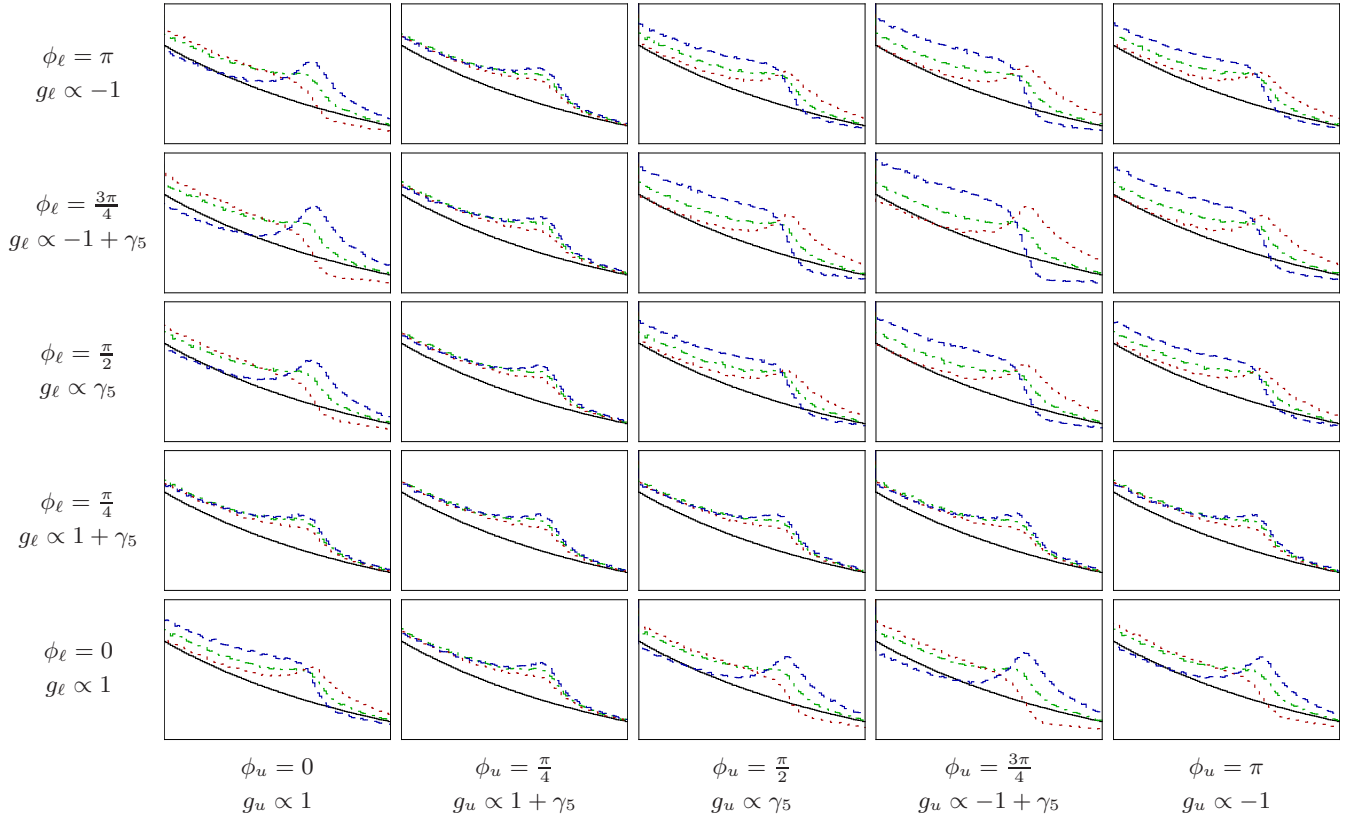


FIG. 7: (Color online) Transverse mass distribution for the process $pp \rightarrow \ell^\pm \nu X$. The vertical axis is the differential cross section in arbitrary units and the horizontal axis is the transverse mass running from 900 GeV to 1050 GeV. The row and column headers specify the nature of the chiral couplings. The curve legends, mass, width, energy and pdf set are the same as in Fig. 2.

especially for the LHC as a symmetric pp collider⁵. Assuming that $\mathbf{p}_{T\nu} = -\mathbf{p}_{T\ell}$, we can solve for $p_{z\nu}$ in terms of the measured charged lepton momentum and the leptonic invariant mass $M_{\ell\nu}$

$$p_{z\nu} = p_{z\ell} \left(\frac{M_{\ell\nu}^2}{2p_{T\ell}^2} - 1 \right) \pm \frac{M_{\ell\nu} E_\ell}{p_{T\ell}} \sqrt{\frac{M_{\ell\nu}^2}{4p_{T\ell}^2} - 1}, \quad (19)$$

where all quantities are in the lab frame. If the width of the new resonance is sufficiently small, then the invariant mass is well approximated by the resonant mass $M_{\ell\nu} \sim M$. With a clear signal identification, the resonance mass could be measured in the transverse mass distribution, just like the M_W determination in the SM. Even so, we still have a two-fold ambiguity in $p_{z\nu}$. On an event-by-event basis, we do not know which one is correct. Instead, for each solution, we can calculate the angle of the charged lepton in the CM frame with respect to the boost direction to approximate the quark moving

direction, formally defined by

$$\cos \theta = \text{sign}(p_{z\ell} + p_{z\nu}) \frac{p_{z\ell}^{CM}}{E_\ell^{CM}}, \quad (20)$$

which in turn also suffers from the above ambiguity. We denote the smaller solution of $|p_{z\nu}|$ by the subscript S and the larger solution by the subscript L . The cosines of these angles in the CM frame, can be expressed by the lab quantities as

$$\begin{aligned} \cos \theta_S &= -\sqrt{1 - \frac{4p_{T\ell}^2}{M^2}} \text{sign} \left(\frac{M}{2} - E_\ell \right), \\ \cos \theta_L &= -\sqrt{1 - \frac{4p_{T\ell}^2}{M^2}}. \end{aligned} \quad (21)$$

When $E_\ell = M/2$, this corresponds to the situation where the lab frame and the CM frame coincide. Both solutions of $\cos \theta$ are identical when $E_\ell \leq M/2$ ⁶. On the other

⁵ Other attempts to reconstruct the spin with a missing particle can be found in [68–83].

⁶ However, there is still the possibility that the boost direction does not coincide with the quark direction as in the neutral current case.

hand, the two solutions differ by a sign when $E_\ell > M/2$. In this latter case, when a wrong solution is chosen, it simply moves the angle from $\cos\theta \rightarrow -\cos\theta$. We show a contour plot of $\cos\theta$ in the $p_{z\ell} - p_{T\ell}$ plane for the two solutions in Fig. 8. As is clear in the plot, $\cos\theta$ does not depend on $p_{z\ell}$ except at the transition point $E_\ell = M/2 = \sqrt{p_{T\ell}^2 + p_{z\ell}^2}$, where it flips sign.

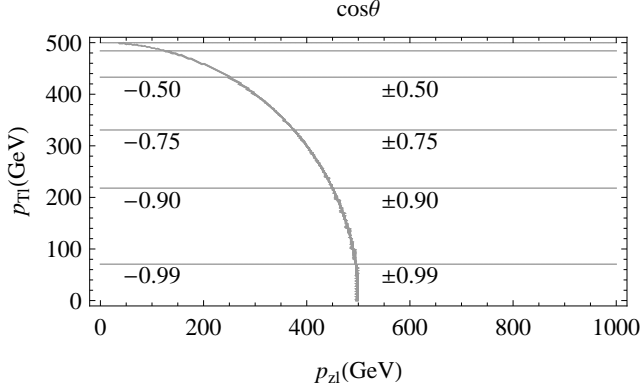


FIG. 8: Contour plot of $\cos\theta$ as a function of the momentum of the charged lepton for the process $pp \rightarrow \ell\nu$. The horizontal lines are the contours. The contours are (starting from the bottom) ± 0.99 , ± 0.90 , ± 0.75 , ± 0.50 , ± 0.25 and 0. The large solution is negative everywhere while the small solution changes sign at the transition point $E_\ell = M/2$ indicated by the circular curve.

These observations lead us to reconstruct adequate angular variables to compensate the loss of information due to the missing neutrino. By taking the large solution $\cos\theta_L$, which is negatively definite, we obtain the distribution $-\cos\theta$. Convoluting with the PDF and imposing the acceptance cuts

$$p_{T\ell} > 250 \text{ GeV}, \quad p_{T\text{miss}} > 250 \text{ GeV}, \quad |\eta_\ell| < 2.5, \quad (22)$$

we reconstruct the angular distributions as seen in the left column of Fig. 9. We further symmetrize the distribution by splitting the large solution in half and taking the mirror image on the $\cos\theta > 0$ side, as seen in the right column of Fig. 9 with the solid (black) curves. With this prescription, we reproduce the correct angular distribution if the true distribution is symmetric (*e.g.*, no parity violation), and we only obtain the average over the positive and negative regions of $\cos\theta$, as compared with the dashed (blue) curves in the right column that present left-left chiral couplings for a vector and a tensor state. In all cases, the spin information is well preserved and this gives us an unambiguous way to determine the spin of a charged boson resonance without the need to reconstruct the CM frame.

On the other hand, the small solution carries both signs and thus contains information not only about the spin, but also the asymmetry. In the region $E_\ell < M/2$, this solution is the same as the large solution and thus the angle is typically correctly reconstructed. In the region

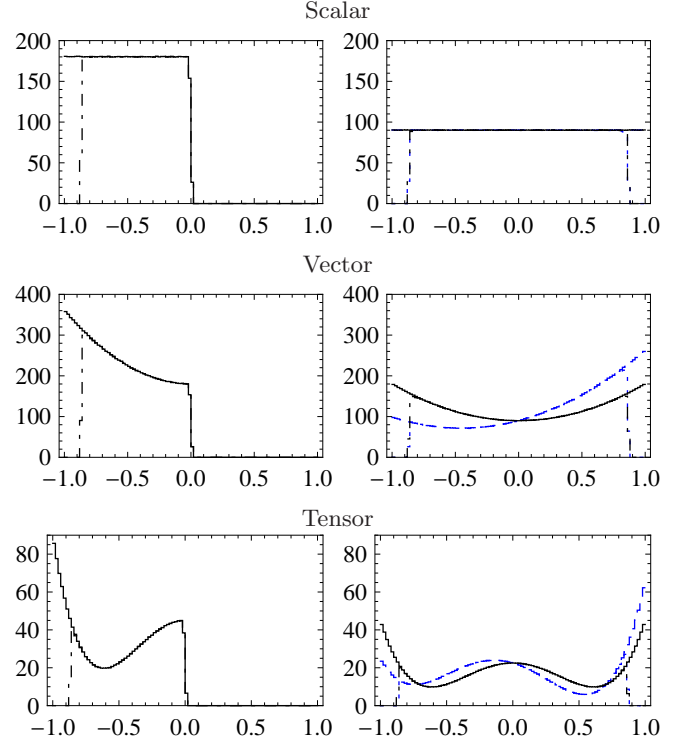


FIG. 9: (Color online) Angular distribution of ℓ for the process $pp \rightarrow \ell\nu$ when only the large solution of the neutrino p_z is taken. The cut-off feature in the forward-backward regions is due to the kinematical cuts as described in the text.

$E_\ell > M/2$, however, either this solution or the one with an opposite sign could be right and we cannot determine it on an event-by-event basis. In each plot in the left column of Fig. 10, we plot the angular distribution using the small solution. The distribution is different for each spin and asymmetry and it generally covers the entire range of $\cos\theta$. As expected, the small solution is essentially correct about $\cos\theta \lesssim -0.6$, but there is a clear deficit when $\cos\theta$ approaches 0^- . The missing events are incorrectly assigned to the bins in $-\cos\theta > 0$, which is also seen as an excess near $\cos\theta \rightarrow 0^+$.

Fortunately, we are able to simulate the expectation and thus restore the distribution on a statistical basis. In each plot on the right column of Fig. 10, the dashed (blue) curve is the expected angular distribution if we know the full momentum information of the neutrino. For $\cos\theta > 0$, we take the difference between the solid (black) curve on the left column and the dashed (blue) curve on the right column, to obtain the excess. We would like to move those events back to the bins in $-\cos\theta < 0$ to restore the original distribution. It is very important to realize that the fractional excess (the above excess divided by the solid (black) curve on the left column) turns out to be numerically the same for all of the scalar, vector and tensor resonances. Denoted by f as a function of $\cos\theta$, we obtain this simulated frac-

tional excess as a universal function for all spins, shown in Fig. 11. This observation leads to a powerful procedure for the restoration of the angular distribution: Given a data set, presumably like the solid (black) curve on the left column, we apply the fractional excess function to the $\cos\theta > 0$ region bin by bin, then subtract this result out from the data, and finally move the result to the region of $\cos\theta < 0$ for the correction.

Plotted on the right column in solid (black) are the corrected angular distributions. In the case of symmetric distributions, the reconstruction works perfectly and the solid (black) curve completely coincides with the expectation of the dashed (blue) line. In the case of asymmetric distributions, the reconstruction is perfect on the edges but slightly off in the middle where the dashed (blue) curve can be seen. This is due to the more likely mismatch between the directions for the true quark momentum and the boost. Nevertheless, it is sufficient to present features of the asymmetry. We reiterate that our correction for each distribution is independent of the resonance spin, although it depends on the parton distribution function as well as the mass of the new resonant particle.

C. Forward-backward asymmetry

The angular distributions for the large solution average out the events and thus lead to no asymmetry. The corrected angular distributions for the small solution as in the right column of Fig. 10 preserve the asymmetry property to a large extent. We could use these angular distributions in the same way as in the neutral current case, or we could use the small solution directly only in the region $|\cos\theta| \gtrsim 0.5$ without performing the $\cos\theta \leftrightarrow -\cos\theta$ correction. Thus similar analyses to Fig. 5 in the neutral currents can be performed. This is a significant progress for the charged boson signal at the LHC as a symmetric collider.

V. SEARCHES FOR DRELL-YAN TYPE SIGNALS AT THE LHC

A. Neutral current channel

The CMS and ATLAS Collaborations have studied dilepton events at 7 TeV in search of a heavy neutral boson [84, 85]. They present their results in terms of the production cross section times branching fraction as a function of mass, which takes into account the couplings, mass and width of the new particle for general spin. In this note, we extend this by projecting the expected 95% confidence level bounds to 10 fb^{-1} at 7 TeV and 10 fb^{-1} and 300 fb^{-1} at 14 TeV. We also place bounds on the product of couplings as a function of mass for each spin while using a standard width.

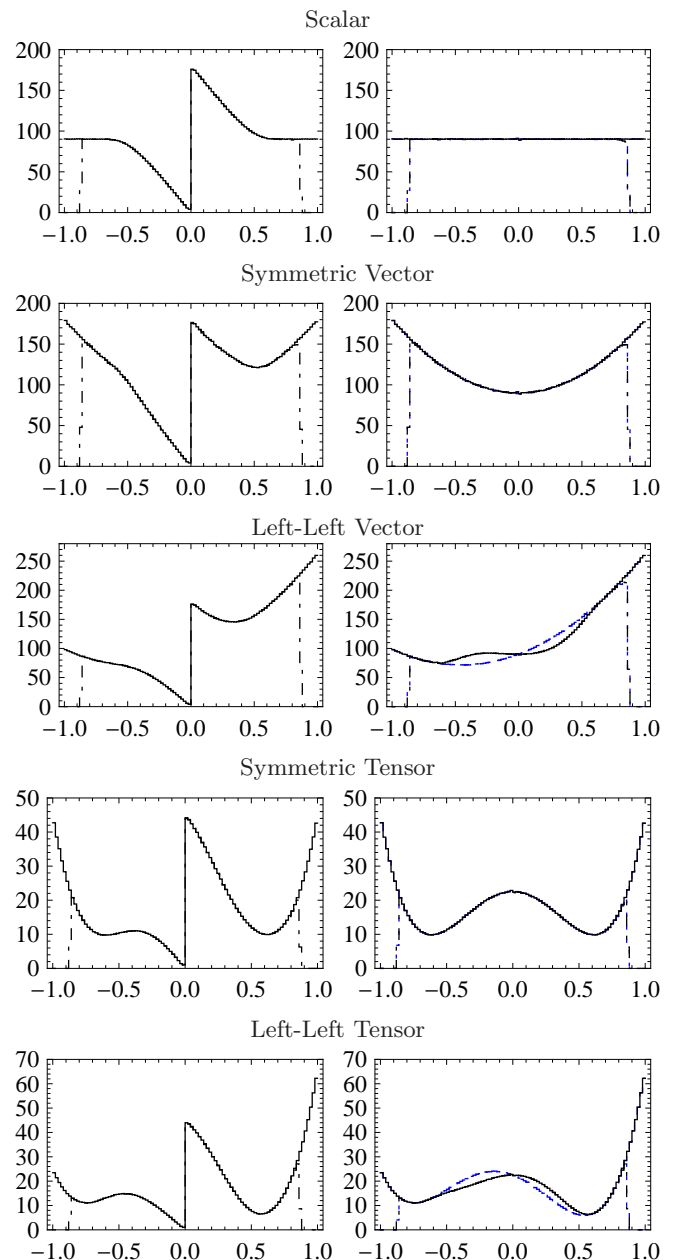


FIG. 10: (Color online) Angular distribution of ℓ for the process $pp \rightarrow \ell \nu$ when only the small solution of the neutrino p_z is taken. Each row lists a case of distinct spin and parity violation. Each plot on the left gives the angular distribution directly obtained from the small solution. On the right, the dashed (blue) curve is the angular distribution with full momentum information of the neutrino. The solid (black) curve is the angular distribution obtained from the corresponding distribution on the left by following the procedure explained in the main text. The cut-off feature in the forward-backward regions is due to the kinematical cuts as described in the text.

We simulate the process $pp \rightarrow \ell^+ \ell^- X$ in the SM at tree level using the parton-level Monte Carlo package CalcHEP [86, 87] and normalize our parton-level calcula-

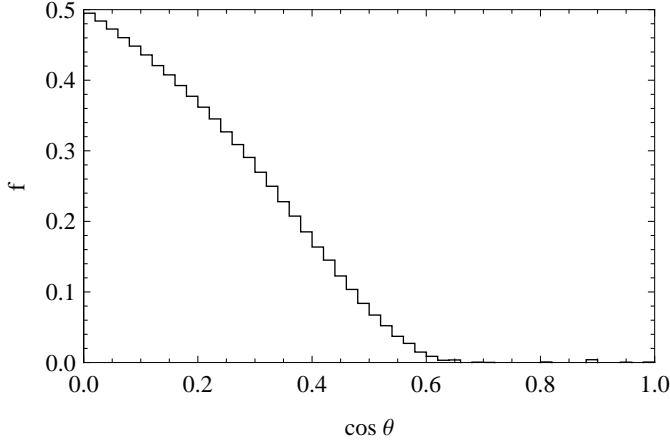


FIG. 11: Fraction of events that should be removed from the $\cos\theta > 0$ side of the small-solution angular distribution and added to the $\cos\theta < 0$ side of the distribution, universal for a charged resonance of any spin.

tions to the data by fitting to the two highest bins (from 85 GeV to 95 GeV) from Fig. 2 of Ref. [84]. Including the numerical normalization factors 0.56 for the e^+e^- channel and 1.01 for the $\mu^+\mu^-$ channel, our results and the CMS data are given in Fig. 12 by the solid (black) curve and the (black) dots, respectively. Signals, including interference with the SM background, corresponding to new resonances of different spins, masses, and fermionic couplings were then done and superimposed on the plot. For simplicity and illustration purposes, we assumed that all the couplings were taken to be real in the numerical studies and that only the first two generations of fermions were taken into account. Results for more general cases are expected to be qualitatively the same.

In numerical estimates of the signal events, the width of the new resonance was taken as 3% of its mass, in line with the assumption made in Ref. [84]. We considered the events in the invariant mass window of $\pm 20\%$ of its mass

$$\frac{4}{5}M \leq M_{\ell\ell} \leq \frac{6}{5}M, \quad (23)$$

where M is the mass of the new particle. The number of events for the e^+e^- and $\mu^+\mu^-$ channels were added ($N = N_e + N_\mu$) to give the total number of predicted events for the SM. This number of events was plugged into the one bin log likelihood [57]

$$LL = 2 \left[N \ln \left(\frac{N}{\nu} \right) + \nu - N \right], \quad (24)$$

where ν is the number of events (for both the e^+e^- and $\mu^+\mu^-$ channels) expected in the SM plus the new boson. A value of $LL = 4$ was taken as the 95% confidence level and ν was solved for. Taking into account the SM expectation and given an available integrated luminosity, this

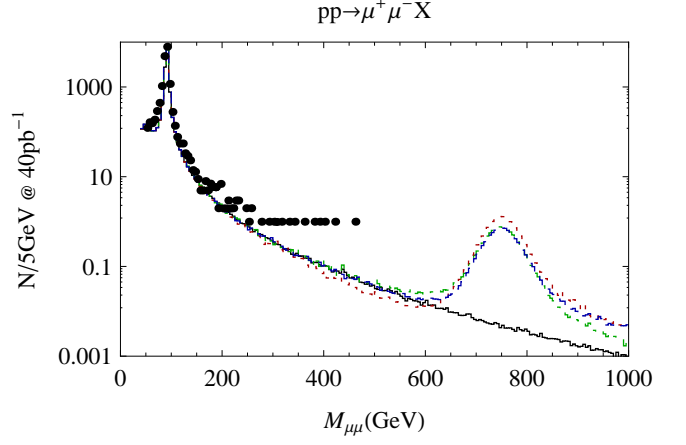


FIG. 12: (Color online) Invariant mass distribution of the charged leptons for the process $pp \rightarrow \mu^+\mu^-X$ at the LHC with 7 TeV. The solid (black) curve is the SM expectation while the dot-dashed (green), dotted (red) and dashed (blue) curves are respectively for spin-0, -1, and -2 resonances with a mass of 750 GeV and a width of 22.5 GeV. The latest CMS data [84] are superimposed in the figure as the (black) dots.

is converted into a signal cross section times the branching fraction for a given mass, and the results are plotted in Fig. 13 for 7 TeV and 14 TeV.

We wish to emphasize that our results here can be broadly applied to any resonant signal as outlined in the earlier sections. The production cross section is governed by the resonant coupling to the initial state partons, and the decay branching fraction is proportional to the coupling to the final state leptons. Thus with the determination of the resonant mass and width by the kinematical peak and the line shape, we expect to gain the information for the fundamental couplings $g_q g_\ell$ for a scalar or a vector resonance, and $g_q g_\ell / \Lambda^2$ for a tensor.

To illustrate this point, we take the commonly studied “sequential Z' model” as an example for a vector resonance (Z'_{SM}), which has the same coupling as the SM Z boson. In Fig. 13, we also include the cross section times branching fraction (the blue dashed curve) for this model as labeled by Z'_{SM} . Where this curve crosses the solid (black) curve gives the bound (or projected bound) for this model. We find a lower bound on Z'_{SM} of 1135 GeV consistent with the CMS results. We also find that CMS could bound the mass at ~ 2.5 TeV with 10 fb^{-1} at 7 TeV, ~ 4.1 TeV with 10 fb^{-1} at 14 TeV and ~ 5.5 TeV with 300 fb^{-1} at 14 TeV. This procedure can easily be applied to other specific models. The couplings and widths simply need to be set and the mass scanned over to determine the cross section times branching fraction.

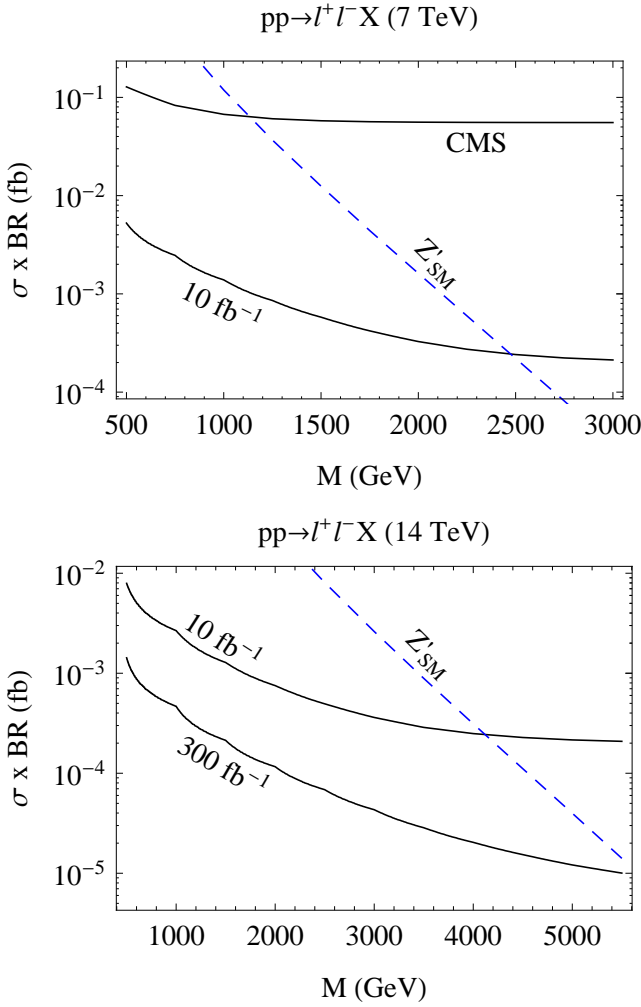


FIG. 13: (Color online) 95% C. L. bound on the production cross section times branching fraction versus the new resonant boson mass. The curve labeled CMS is with respect to the data measured by the CMS Collaboration [84], while the other solid (black) curves are projections for the specified integrated luminosity. The dashed (blue) curve is for a Z' with the same couplings as the SM Z .

B. Charged current channel

Following the same procedure as in the previous section, we calculate the 95% confidence level bounds and projected bounds on a new charged resonant boson. We base our results on the the CMS data published in [88, 89]. We simulate $pp \rightarrow \ell\nu$ ($\ell = e, \mu$) in the SM at tree level, again using the parton-level Monte Carlo package CalcHEP, and normalize our parton-level calculations to the data by multiplying our simulation with a numerical factor which brings the two highest bins (from 50 GeV to 100 GeV) into agreement. We found the numerical factor to be 0.76 for the electron and 0.91 for the muon. A plot of our SM calculation and the CMS data can be seen in Fig. 14 where the solid (black) line is the parton-level

prediction of the SM and the (black) dots are the CMS data for the case of the muon.

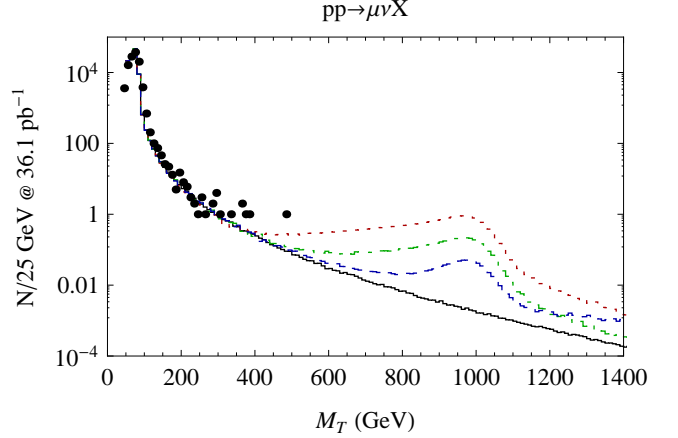


FIG. 14: (Color online) Transverse mass distribution of the charged lepton at the LHC with 7 TeV. The solid (black) curve is the SM expectation while the dot-dashed (green), dotted (red) and dashed (blue) curves are respectively for spin-0, -1, and -2 resonances with a mass of 1 TeV and a width of 20 GeV. The latest CMS data [89] are superimposed as the (black) dots.

The significance was calculated by taking the number of events in the window

$$\frac{2}{5}M < M_T < \frac{6}{5}M. \quad (25)$$

The one bin log likelihood was then calculated for the sum of the electron case and the muon case.

We again plotted the $LL = 4$ line as the 95% confidence level in Fig. 15. Once again, to illustrate the approach to generalize to other models, we plot the cross section times branching fraction of a new charged vector boson with the same couplings as that in the SM, the “sequential W' model”, denoted by W'_{SM} . We find that W'_{SM} is bound to be heavier than 1500 GeV at 95% confidence level which is close to the CMS result [88]. We also find that CMS could achieve a bound of ~ 2.5 TeV with 10 fb^{-1} at 7 TeV, a bound of ~ 4.5 TeV with 10 fb^{-1} at 14 TeV and a bound of ~ 5.2 TeV with 300 fb^{-1} at 14 TeV. We again note that this procedure can be followed with any models. After the couplings and widths are set appropriately, the cross section times branching fraction can be calculated and plotted as a function of mass.

VI. SUMMARY

We have considered the most general new resonant s -channel contributions to Drell-Yan production of leptons at the LHC including spin-0, 1 and 2 bosons. We formulated the most general leading-order interactions between these new particles and the SM fields involved in the DY

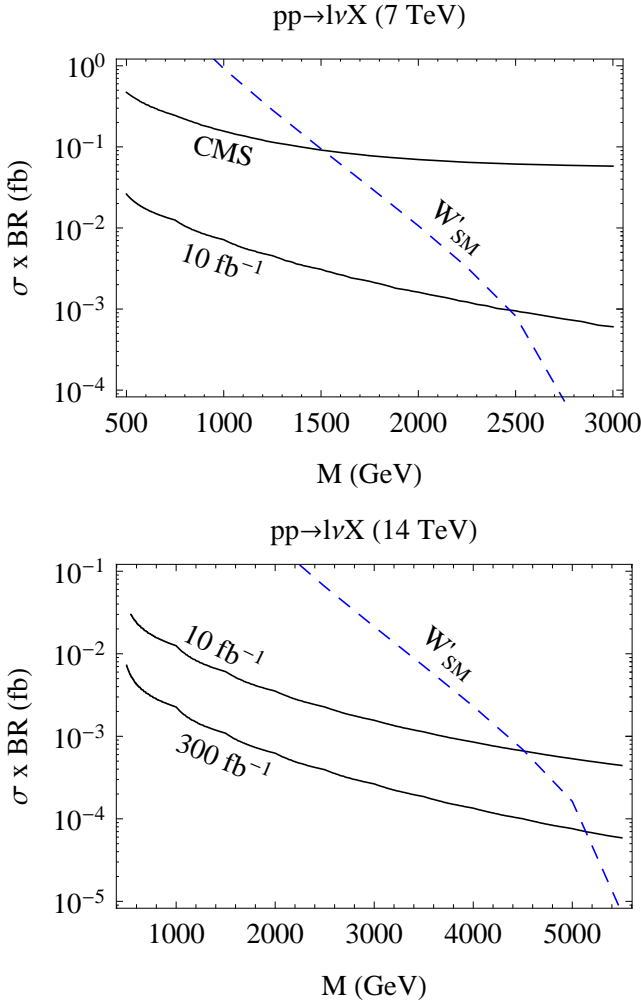


FIG. 15: (Color online) 95% C. L. bound on the production cross section times branching fraction versus the new resonant boson mass. The curve labeled CMS is with respect to the data measured by the CMS Collaboration [88, 89], while the other solid (black) curves are projections for the specified integrated luminosity. The dashed (blue) curve is for a W' with the same couplings as the SM W .

channel that satisfy Lorentz and EM invariances including both parity conserving and violating terms. Using these interactions, we have calculated the helicity amplitudes and expressed them in terms of the Wigner $d^j_{m,m'}$ functions, explicitly showing the angular dependence of these collisions in the CM frame.

For the neutral current process $pp \rightarrow \ell^+ \ell^- X$, we find that

- the lepton pair invariant mass distribution may provide information for the chiral interactions. A new spin-1 field interferes with the SM process, thus modifying its shape from the Breit-Wigner resonance and the position of its peak, while both spin-0 and spin-2 fields do not have significant interference with the SM and appear as simple Breit-

Wigner resonances.

- the transverse momentum of the charged lepton also provides information for the chiral interactions. Both the spin-1 and spin-2 fields present interference with the SM background. Along with the invariant mass distribution, this gives another way to distinguish between the spins.
- defining an angle of ℓ^- with respect to the boost direction (likely to be the initial quark direction) in the CM frame of the system, one is able to construct the Wigner $d^j_{m,m'}$ functions as well as their asymmetry due to parity violation. We note that an asymmetry only occurs for a spin-1 or 2 boson when both the quark coupling and the lepton coupling are not either purely vectorial (tensorial) or axial vector (axial tensor) and is maximized when the vectorial (tensorial) and axial (axial tensor) couplings are equal in magnitude.
- although it is well-known that a chiral spin-1 boson generates an asymmetry when the forward and backward directions are defined in the full angular range from $0 < \cos \theta < 1$ and $-1 < \cos \theta < 0$, respectively, the tensor asymmetry would be zero if taking this range. Instead, we find that the asymmetry is maximized for the tensor when considering the asymmetry in the range $1/\sqrt{2} < \cos \theta < 1$ and $-1 < \cos \theta < -1/\sqrt{2}$, respectively. Thus the asymmetry gives a new way to distinguish between the spins.
- scanning over mass and cross section times branching fraction for the new bosons, we obtained the 95% confidence level bounds based on the current CMS results as well as projected bounds for future integrated luminosities and machine energies. To illustrate how to apply our formulation and calculation to other DY resonances, we plotted the cross section times branching fraction as a function of mass for a new vector boson with the same couplings as the SM Z boson (denoted by Z'_{SM}).

For the charged current process $pp \rightarrow \ell^\pm \nu X$, we find that

- the $\ell \nu$ transverse mass distribution may provide information for the chiral interactions. Spin-1 and spin-2 fields interfere with the SM process, thus modifying its shape from the conventional noninterfering transverse mass distribution as well as the position of the Jacobian peak while a spin-0 field does not have significant interference with the SM and appears with the conventional shape. The shifted position of the peak can be important in determining the mass of the new resonance.
- although determining the angle of ℓ^\pm with respect to the boost direction is more challenging due to the

two-fold ambiguity in the z -component of the neutrino momentum, we find a novel statistical method for reconstructing the angular distribution. This method involves creating two distributions, one for the small neutrino z -component momentum and another for the large neutrino z -component momentum. We find that the large solution faithfully preserves the symmetrized Wigner $d_{m,m'}^j$ function and therefore fully determines the spin of the new resonance but not the asymmetry. The small solution distribution, on the other hand, does contain information about the asymmetry and we show how that information can be extracted.

- scanning over mass and cross section times branching fraction for the new bosons, we obtained the 95% confidence level bounds based on the current CMS results as well as projected bounds for future integrated luminosities and machine energies. To illustrate how to apply our formulation and calculation to other DY resonances, we plotted the cross section times branching fraction as a function of mass for a new vector boson with the same couplings as the SM W boson (denoted W'_{SM}).

We would like to reiterate that our formulation makes the future phenomenological and experimental searches straightforward. Our proposal for the large and small solutions for the charged current channel overcomes the difficulty of the two-fold ambiguity due to the missing neutrinos, that should be adopted for studies of new charged resonances.

Acknowledgments

We would like to thank Camilo Garcia for discussions. C.W.C was supported by NSC Grant No. 97-2112-M-008-002-MY3. N.D.C. is supported by the US National Science Foundation, grant NSF-PHY-0705682, the LHC Theory Initiative. G.J.D. is supported by the National Natural Science Foundation of China under Grant No.10905053. T.H. is supported in part by the U.S. Department of Energy under grant No. DE-FG02-95ER40896.

Appendix A: Feynman Rules

In this appendix, we provide the Feynman rules used in the analyses. The interaction vertices between the neutral resonances and the SM fields are listed in Fig. 16. The interaction vertices between the charged resonances and the SM fermions are listed in Fig. 17. The relevant SM vertices are reproduced in Fig. 18 to fix our convention.

Appendix B: FeynRules Implementation

We implemented our formulation using the FeynRules Mathematica package [90]. We will make the FeynRules model files available through the FeynRules model database where those who are interested can download and use it. We briefly describe this implementation in this section.

This implementation uses two FeynRules model files. The first is the SM that comes with FeynRules (“SM.fr”), although we will include a copy of this file in case changes are made to the SM model files later. We added all the new particles, parameters and Lagrangian terms to a new file we call “plus.fr”.

The names of the particles along with their charge, mass and width are listed in Table IV. These are the

	Name	Mass	Width
S	SV	MSV	WSV
V_μ	VV	MVV	WVV
$T_{\mu\nu}$	TV	MTV	WTV
S^\pm	SVP \pm	MSVP	WSVP
V_μ^\pm	VVP \pm	MVVP	WVVP
$T_{\mu\nu}^\pm$	TVP \pm	MTVP	WTVP

TABLE IV: Particles implemented in FeynRules. In the first column is the symbol we use for the particle in this article. In the last 3 columns are the ASCII names we use for these particles, their masses and widths in FeynRules. These are the names that would be used in a simulation. The masses are set to 1 TeV by default while the widths are set to be 20 GeV by default, but both of these parameters are free and can be set by the user.

names that are used when running a Monte Carlo program.

The couplings are implemented with names that are similar to the ones we use in this article. However, there is a six-character limit in CalcHEP for the names of parameters, so some names are shortened. We list the parameter names in Table V. The couplings are implemented in a very general way in the FeynRules file and are all set to zero by default so that the user can turn on the vertices that they are interested in. Some are removed from the Monte Carlo file using “Definitions” in the FeynRules model file. These can easily be turned on by removing the appropriate definitions (the full couplings are included in the Lagrangians), but the user should remember the hermiticity requirements on some of the couplings. Furthermore, if the user desires to use this implementation with a Monte Carlo package that can handle complex parameters, it is possible to turn off the splitting of these couplings into real and imaginary parts by commenting out the “Definitions” line of the complex couplings.

The full Lagrangians described in this article were included in the FeynRules model files. FeynRules was then

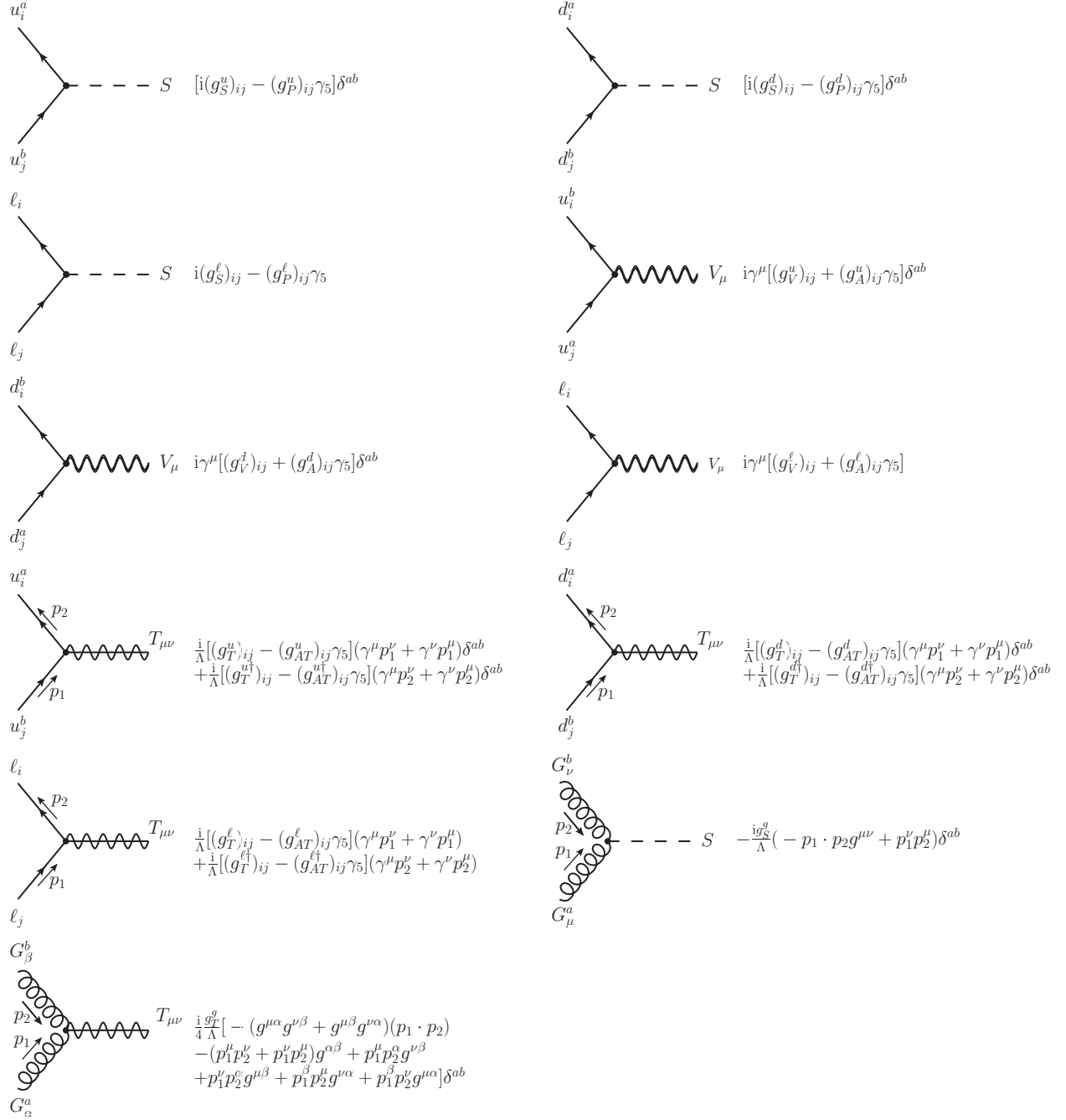


FIG. 16: Interaction vertices between the new bosons and SM fields.

run on this file and all the resulting vertices were checked against our independent calculations of these vertices and agreement was found.

The CalcHEP interface [91] was then run on this model, which generated a set of CalcHEP model files. We used CalcHEP to generate the analytic formulas for the squared matrix element for all the $2 \rightarrow 2$ Drell-Yan processes where we only included the first generation fermions. We checked these formulas against our own independent calculations of these squared matrix elements

and found agreement. We then used these model files to do the numerical studies described in this article.

These model files are intended to be used in unitary gauge and below the effective cutoff of these vertices. Furthermore, these interactions are not ultraviolet complete and should not be used for other processes than the Drell-Yan processes described here.

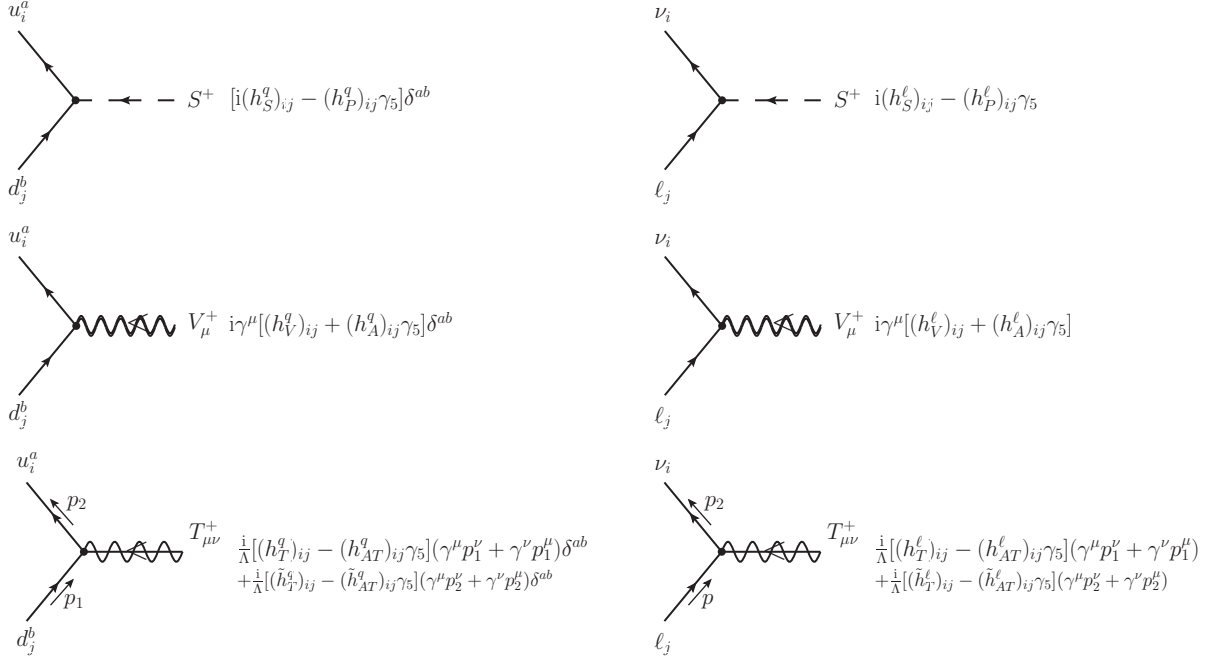


FIG. 17: Interaction vertices between the new charged bosons and SM fermions.

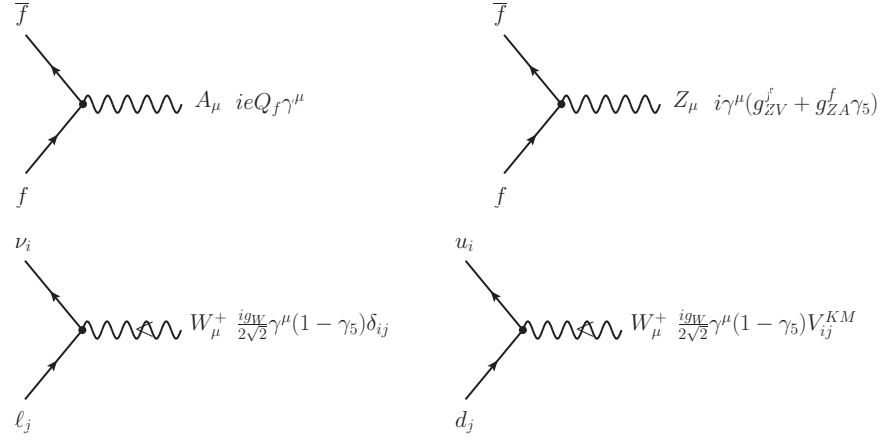


FIG. 18: Interaction vertices between the SM gauge bosons and fermions, where the weak coupling \$g_W\$ is related to the Fermi constant \$G_F\$ by \$\frac{G_F}{\sqrt{2}} = \frac{g_W^2}{8M_W^2}\$.

Appendix C: \$d_{m,m'}^j\$ Function Review

In this appendix, we briefly review the Wigner \$d_{m,m'}^j\$ functions. Suppose the incoming state has total angular momentum \$j\$ and total spin \$m\$ along the direction of motion of one of the particles. We will call this the \$z\$-direction and the total spin is the difference of the par-

ticles' helicities⁷. The final state has the same total angular momentum and spin \$m'\$ along the direction of motion of one of the final state particles and at an angle \$\theta\$ with respect to the \$z\$-direction. We will define the \$x\$-direction such that the whole process occurs in the \$x\$-\$z\$ plane. The spin along this direction is the difference of helicity of the

⁷ Although orbital angular momentum plays a role, it's \$z\$-component is 0. As a result, the total angular momentum \$z\$-component is equal to the spin \$z\$-component (\$j_z = m\$).

	Name	Real part	Imaginary part
g_{Sij}^f	gSfij	gSfRij	gSfIij
g_{Pij}^f	gPfij	gPfRij	gPfIij
g_S^g	gSg		
g_{Vij}^f	gVfij	gVfRij	gVfIij
g_{Aij}^f	gAfij	gAfRij	gAfIij
g_V^g	gVg		
g_{Tij}^f/Λ	gTfij	gTfRij	gTfIij
g_{ATij}^f/Λ	gUfij	gUfRij	gUfIij
g_T^g/Λ	gTg		
h_{Sij}^f	hSfij	hSfRij	hSfIij
h_{Pij}^f	hPfij	hPfRij	hPfIij
h_{Vij}^f	hVfij	hVfRij	hVfIij
h_{Aij}^f	hAfij	hAfRij	hAfIij
h_{Tij}^f/Λ	hTfij	hTfRij	hTfIij
h_{ATij}^f/Λ	hUfij	hUfRij	hUfIij
$\tilde{h}_{Tij}^f/\Lambda$	hYfij	hYfRij	hYfIij
$\tilde{h}_{ATij}^f/\Lambda$	hZfij	hZfRij	hZfIij

TABLE V: Couplings implemented in FeynRules. In the first column is the symbol we use for the coupling in this article. In the second column is the ASCII name we use for this coupling in FeynRules while the third and fourth columns contain the the real and imaginary parts. The letter “f” refers to the flavor and runs over “u”, “d” and “l” for the neutral current couplings while it runs over “q” and “l” for the charged current couplings. The i and j stand for the generation.

final state particles. With these definitions, the $d_{m,m'}^j$ function is defined as the overlap between the incoming and outgoing states

$$d_{m,m'}^j(\theta) = \langle j, m', \theta | j, m \rangle = \langle j, m' | e^{iJ_y \theta} | j, m \rangle, \quad (C1)$$

where we have extracted the angular dependence into the operator $\exp(iJ_y \theta)$ which rotates the final state around the y -axis to an angle θ with respect to the z -axis. Commonly used functions are listed in Table VI. For $j = 0$,

the generator of rotations around the y -axis is $J_y = 0$ and so

$$d_{0,0}^0(\theta) = 1. \quad (C2)$$

For $j = 1$, the generator J_y is

$$J_y = \frac{-i}{\sqrt{2}} \begin{pmatrix} 0 & 1 & 0 \\ -1 & 0 & 1 \\ 0 & -1 & 0 \end{pmatrix}. \quad (C3)$$

We also find that

$$J_y^2 = \frac{-1}{2} \begin{pmatrix} -1 & 0 & 1 \\ 0 & -2 & 0 \\ 1 & 0 & -1 \end{pmatrix} \quad (C4)$$

$$\begin{aligned} d_{0,0}^0 &= 1 \\ d_{1,\pm 1}^1 &= \frac{1}{2}(1 \pm \cos \theta) \\ d_{1,\pm 1}^2 &= \frac{1}{2}(1 \pm \cos \theta)(2 \cos \theta \mp 1) \\ d_{2,\pm 1}^2 &= -\frac{1}{2}(1 \pm \cos \theta) \sin \theta \end{aligned}$$

TABLE VI: Wigner $d_{m,m'}^j$ functions relevant for our processes and used in the helicity amplitudes given in Tables II and III.

and

$$J_y^{2n} = J_y^2, \quad J_y^{2n+1} = J_y, \quad (C5)$$

where $n > 0$. With this information, $\exp(iJ_y \theta)$ can be expanded and it can be shown that

$$d_{m,m'}^1 = e^{iJ_y \theta} = \begin{pmatrix} \frac{1}{2}(1 + \cos \theta) & \frac{1}{\sqrt{2}} \sin \theta & \frac{1}{2}(1 - \cos \theta) \\ -\frac{1}{\sqrt{2}} \sin \theta & \cos \theta & \frac{1}{\sqrt{2}} \sin \theta \\ \frac{1}{2}(1 - \cos \theta) & \frac{1}{\sqrt{2}} \sin \theta & \frac{1}{2}(1 + \cos \theta) \end{pmatrix}, \quad (C6)$$

where m and m' refer to the elements of the matrix.

-
- [1] For recent reviews on Z' and W' searches, see, e.g., M.-C. Chen and B.A. Dobrescu, in K. Nakamura *et al.* [Particle Data Group Collaboration], J. Phys. G **G37**, 075021 (2010).
- [2] F. del Aguila, M. Quiros, F. Zwirner, Nucl. Phys. **B287**, 419 (1987).
- [3] V. D. Barger, N. G. Deshpande, J. L. Rosner, K. Whisnant, Phys. Rev. **D35**, 2893 (1987)
- [4] U. Baur, K. H. Schwarzer, Phys. Lett. **B180**, 163 (1986).
- [5] P. Langacker, M. -x. Luo, Phys. Rev. **D45**, 278-292 (1992).
- [6] F. del Aguila, M. Cvetič, P. Langacker, Phys. Rev. **D48**, 969-973 (1993). [hep-ph/9303299].
- [7] P. Abreu *et al.* [DELPHI Collaboration], Z. Phys. **C65**, 603-618 (1995).
- [8] S. Riemann, [hep-ph/9610513].
- [9] A. Leike, Phys. Rept. **317**, 143-250 (1999). [hep-ph/9805494].
- [10] H. Davoudiasl, J. L. Hewett, T. G. Rizzo, Phys. Rev. **D63**, 075004 (2001). [hep-ph/0006041].
- [11] B. C. Allanach, K. Odagiri, M. A. Parker, B. R. Webber, JHEP **0009**, 019 (2000). [hep-ph/0006114].
- [12] T. G. Rizzo, JHEP **0306**, 021 (2003). [hep-ph/0305077].
- [13] M. Dittmar, A. -S. Nicollerat, A. Djouadi, Phys. Lett. **B583**, 111-120 (2004). [hep-ph/0307020].
- [14] M. S. Carena, A. Daleo, B. A. Dobrescu, T. M. P. Tait, Phys. Rev. **D70**, 093009 (2004). [hep-ph/0408098].
- [15] P. Burikham, T. Figy, T. Han, Phys. Rev. **D71**, 016005

- (2005). [hep-ph/0411094].
- [16] T. G. Rizzo, [hep-ph/0610104].
- [17] A. Djouadi, G. Moreau, R. K. Singh, Nucl. Phys. **B797**, 1-26 (2008). [arXiv:0706.4191 [hep-ph]].
- [18] K. Agashe, H. Davoudiasl, S. Gopalakrishna, T. Han, G. -Y. Huang, G. Perez, Z. -G. Si, A. Soni, Phys. Rev. **D76**, 115015 (2007). [arXiv:0709.0007 [hep-ph]].
- [19] B. Fuks, M. Klasen, F. Ledroit, Q. Li, J. Morel, Nucl. Phys. **B797**, 322-339 (2008). [arXiv:0711.0749 [hep-ph]].
- [20] P. Langacker, Rev. Mod. Phys. **81**, 1199-1228 (2009). [arXiv:0801.1345 [hep-ph]].
- [21] F. Petriello, S. Quackenbush, Phys. Rev. **D77**, 115004 (2008). [arXiv:0801.4389 [hep-ph]].
- [22] C. Coriano, A. E. Faraggi, M. Guzzi, Phys. Rev. **D78**, 015012 (2008). [arXiv:0802.1792 [hep-ph]].
- [23] H. Davoudiasl, G. Perez, A. Soni, Phys. Lett. **B665**, 67-71 (2008). [arXiv:0802.0203 [hep-ph]].
- [24] F. J. Petriello, S. Quackenbush, K. M. Zurek, Phys. Rev. **D77**, 115020 (2008). [arXiv:0803.4005 [hep-ph]].
- [25] Y. Gershtein, F. Petriello, S. Quackenbush, K. M. Zurek, Phys. Rev. **D78**, 095002 (2008). [arXiv:0809.2849 [hep-ph]].
- [26] T. G. Rizzo, JHEP **0908**, 082 (2009). [arXiv:0904.2534 [hep-ph]].
- [27] P. Osland, A. A. Pankov, A. V. Tsytrinov, N. Paver, Phys. Rev. **D79**, 115021 (2009). [arXiv:0904.4857 [hep-ph]].
- [28] J. Erler, P. Langacker, S. Munir, E. R. Pena, JHEP **0908**, 017 (2009). [arXiv:0906.2435 [hep-ph]].
- [29] Y. Li, F. Petriello, S. Quackenbush, Phys. Rev. **D80**, 055018 (2009). [arXiv:0906.4132 [hep-ph]].
- [30] E. Salvioni, G. Villadoro, F. Zwirner, JHEP **0911**, 068 (2009). [arXiv:0909.1320 [hep-ph]].
- [31] R. Diener, S. Godfrey, T. A. W. Martin, [arXiv:0910.1334 [hep-ph]].
- [32] For a recent review, see, for example, P. Langacker, [arXiv:0911.4294 [hep-ph]].
- [33] F. del Aguila, J. de Blas, M. Perez-Victoria, JHEP **1009**, 033 (2010). [arXiv:1005.3998 [hep-ph]].
- [34] E. Accomando, A. Belyaev, L. Fedeli, S. F. King, C. Shepherd-Themistocleous, Phys. Rev. **D83**, 075012 (2011). [arXiv:1010.6058 [hep-ph]].
- [35] T. Abe, T. Masubuchi, S. Asai, J. Tanaka, [arXiv:1103.3579 [hep-ph]].
- [36] W. Y. Keung and G. Senjanovic, Phys. Rev. Lett. **50**, 1427 (1983).
- [37] J. M. Frere, W. W. Repko, Phys. Lett. **B254**, 485-488 (1991).
- [38] Z. Sullivan, Phys. Rev. **D66**, 075011 (2002). [hep-ph/0207290].
- [39] A. Birkedal, K. Matchev, M. Perelstein, Phys. Rev. Lett. **94**, 191803 (2005). [hep-ph/0412278].
- [40] K. Agashe, S. Gopalakrishna, T. Han, G. -Y. Huang, A. Soni, Phys. Rev. **D80**, 075007 (2009). [arXiv:0810.1497 [hep-ph]].
- [41] S. Gopalakrishna, T. Han, I. Lewis, Z. -g. Si, Y. -F. Zhou, Phys. Rev. **D82**, 115020 (2010). [arXiv:1008.3508 [hep-ph]].
- [42] M. Frank, A. Hayreter, I. Turan, Phys. Rev. **D83**, 035001 (2011). [arXiv:1010.5809 [hep-ph]].
- [43] M. Schmaltz and C. Spethmann, JHEP **1107**, 046 (2011) [arXiv:1011.5918 [hep-ph]].
- [44] C. Grojean, E. Salvioni, R. Torre, JHEP **1107**, 002 (2011). [arXiv:1103.2761 [hep-ph]].
- [45] E. Accomando, D. Becciolini, S. De Curtis, D. Dominici, L. Fedeli, [arXiv:1107.4087 [hep-ph]].
- [46] P. Langacker, R. W. Robinett, J. L. Rosner, Phys. Rev. **D30**, 1470 (1984).
- [47] M. Cvetič, S. Godfrey, in Barklow, T.L. (ed.) et al.: Electroweak symmetry breaking and new physics at the TeV scale 383-415. [hep-ph/9504216].
- [48] H. -C. Cheng, K. T. Matchev, M. Schmaltz, Phys. Rev. **D66**, 056006 (2002). [hep-ph/0205314].
- [49] T. Han, H. E. Logan, B. McElrath, L. -T. Wang, Phys. Rev. **D67**, 095004 (2003). [hep-ph/0301040].
- [50] T. Han, H. E. Logan, L. -T. Wang, JHEP **0601**, 099 (2006). [hep-ph/0506313].
- [51] K. Agashe, A. Belyaev, T. Krupovnickas, G. Perez, J. Virzi, Phys. Rev. **D77**, 015003 (2008). [hep-ph/0612015].
- [52] R. S. Chivukula, N. D. Christensen, E. H. Simmons, Phys. Rev. **D77**, 035001 (2008). [arXiv:0712.0546 [hep-ph]].
- [53] J. Alwall, P. Schuster, N. Toro, Phys. Rev. **D79**, 075020 (2009). [arXiv:0810.3921 [hep-ph]].
- [54] O. Cata, G. Isidori, J. F. Kamenik, Nucl. Phys. **B822**, 230-244 (2009). [arXiv:0905.0490 [hep-ph]].
- [55] R. Barbieri, A. E. Carcamo Hernandez, G. Corcella, R. Torre, E. Trincherini, JHEP **1003**, 068 (2010). [arXiv:0911.1942 [hep-ph]].
- [56] X. -P. Wang, Y. -K. Wang, B. Xiao, J. Xu, S. -h. Zhu, Phys. Rev. **D83**, 117701 (2011). [arXiv:1104.1161 [hep-ph]].
- [57] G. Cowan in K. Nakamura *et al.* [Particle Data Group Collaboration], J. Phys. G **G37**, 075021 (2010).
- [58] J. Pumplin, D. R. Stump, J. Huston, H. L. Lai, P. M. Nadolsky and W. K. Tung, JHEP **0207**, 012 (2002) [arXiv:hep-ph/0201195].
- [59] P. Ferrario and G. Rodrigo, Phys. Rev. D **78**, 094018 (2008) [arXiv:0809.3354 [hep-ph]].
- [60] J. L. Hewett, J. Shelton, M. Spannowsky, T. M. P. Tait and M. Takeuchi, arXiv:1103.4618 [hep-ph].
- [61] J. L. Rosner, Phys. Rev. **D35**, 2244 (1987).
- [62] S. Godfrey, J. L. Hewett, T. G. Rizzo, Phys. Rev. **D37**, 643 (1988).
- [63] J. L. Rosner, Phys. Rev. **D54**, 1078-1082 (1996). [hep-ph/9512299].
- [64] M. Dittmar, Phys. Rev. **D55**, 161-166 (1997). [hep-ex/9606002].
- [65] Y. -k. Wang, B. Xiao, S. -h. Zhu, Phys. Rev. **D83**, 015002 (2011). [arXiv:1011.1428 [hep-ph]].
- [66] Z. -q. Zhou, B. Xiao, Y. -k. Wang, S. -h. Zhu, Phys. Rev. **D83**, 094022 (2011). [arXiv:1102.1044 [hep-ph]].
- [67] T. G. Rizzo, JHEP **0705**, 037 (2007). [arXiv:0704.0235 [hep-ph]].
- [68] For a recent review, see, for example, L. -T. Wang, I. Yavin, Int. J. Mod. Phys. **A23**, 4647-4668 (2008). [arXiv:0802.2726 [hep-ph]].
- [69] A. J. Barr, Phys. Lett. **B596**, 205-212 (2004). [hep-ph/0405052].
- [70] J. M. Smillie, B. R. Webber, JHEP **0510**, 069 (2005). [hep-ph/0507170].
- [71] A. Datta, K. Kong, K. T. Matchev, Phys. Rev. **D72**, 096006 (2005). [hep-ph/0509246].
- [72] A. J. Barr, JHEP **0602**, 042 (2006). [hep-ph/0511115].
- [73] R. Cousins, J. Mumford, J. Tucker, V. Valuev, JHEP **0511**, 046 (2005).
- [74] C. Athanasiou, C. G. Lester, J. M. Smillie, B. R. Webber,

- JHEP **0608**, 055 (2006). [hep-ph/0605286].
- [75] L. -T. Wang, I. Yavin, JHEP **0704**, 032 (2007). [hep-ph/0605296].
 - [76] J. M. Smillie, Eur. Phys. J. **C51**, 933-943 (2007). [hep-ph/0609296].
 - [77] O. Antipin, A. Soni, JHEP **0810**, 018 (2008). [arXiv:0806.3427 [hep-ph]].
 - [78] O. Gedalia, S. J. Lee, G. Perez, Phys. Rev. **D80**, 035012 (2009). [arXiv:0901.4438 [hep-ph]].
 - [79] F. Boudjema, R. K. Singh, JHEP **0907**, 028 (2009). [arXiv:0903.4705 [hep-ph]].
 - [80] L. Edelhauser, W. Porod, R. K. Singh, JHEP **1008**, 053 (2010). [arXiv:1005.3720 [hep-ph]].
 - [81] H. -C. Cheng, Z. Han, I. -W. Kim, L. -T. Wang, JHEP **1011**, 122 (2010). [arXiv:1008.0405 [hep-ph]].
 - [82] G. Moortgat-Pick, K. Rolbiecki, J. Tattersall, Phys. Lett. **B699**, 158-163 (2011). [arXiv:1102.0293 [hep-ph]].
 - [83] O. J. P. Eboli, C. S. Fong, J. Gonzalez-Fraile, M. C. Gonzalez-Garcia, Phys. Rev. **D83**, 095014 (2011). [arXiv:1102.3429 [hep-ph]].
 - [84] S. Chatrchyan *et al.* [CMS Collaboration], arXiv:1103.0981 [hep-ex].
 - [85] G. Aad *et al.* [ATLAS Collaboration], Phys. Lett. **B700**, 163-180 (2011). [arXiv:1103.6218 [hep-ex]].
 - [86] A. Pukhov, [hep-ph/0412191].
 - [87] A. Pukhov, E. Boos, M. Dubinin, V. Edneral, V. Ilyin, D. Kovalenko, A. Kryukov, V. Savrin *et al.*, [hep-ph/9908288].
 - [88] V. Khachatryan *et al.* [CMS Collaboration], arXiv:1012.5945 [hep-ex];
 - [89] S. Chatrchyan *et al.* [CMS Collaboration], arXiv:1103.0030 [hep-ex].
 - [90] N. D. Christensen, C. Duhr, Comput. Phys. Commun. **180**, 1614-1641 (2009). [arXiv:0806.4194 [hep-ph]].
 - [91] N. D. Christensen, P. de Aquino, C. Degrande, C. Duhr, B. Fuks, M. Herquet, F. Maltoni, S. Schumann, Eur. Phys. J. **C71**, 1541 (2011). [arXiv:0906.2474 [hep-ph]].